Atomic chains on surfaces

2008 J. Phys.: Condens. Matter 20 393001

(http://iopscience.iop.org/0953-8984/20/39/393001)

IOP PUBLISHING JOURNAL OF PHYSICS: CONDENSED MATTER

J. Phys.: Condens. Matter **20** (2008) 393001 (26pp) doi:10.1088/0953-8984/20/39/393001

TOPICAL REVIEW

Atomic chains on surfaces

Nuri Oncel

Department of Chemistry, Princeton University, Princeton, NJ 08544, USA

Received 9 March 2008, in final form 17 June 2008
Published 19 August 2008
Online at stacks.iop.org/JPhysCM/20/393001

Abstract

The physical and electronic properties of atomic chains formed on various surfaces have become one of the most popular fields of study in surface science. Due to the inherent one-dimensional nature of these chains, various exotic physical phenomena specific to one-dimensional systems have been observed. Among them are Peierls instability and Luttinger liquid behavior. This topical review briefly introduces the physics of these one-dimensional atomic chains and gives some examples from the recently published literature.

(Some figures in this article are in colour only in the electronic version)

Contents

1. Introduction

Technological development in the fabrication of integrated circuits suggests that in the near future the typical size of the individual components of these circuits will be scaled down from tens of nanometers to only a few nanometers. As it becomes possible to engineer such components, the next step will be the connection of these pieces in order to incorporate them into the circuit. Ideally speaking, this connection could be scaled down to wires of only one atom in diameter. Therefore, the fabrication of these connections and their physical properties are as important as the individual components. Today it is possible to create well defined low-dimensional structures on the nanometer scale by using various techniques [1]. Besides the technological necessities of producing these atomic chains, they are valuable substrates for the study of rather interesting properties of one-dimensional physics such as Peierls instability [2] and Luttinger liquids [3].

Advances in scanning probe techniques allow the addressing and manipulation of individual atoms. Artificial structures can be built by using these individual atoms. Particularly beautiful and pioneering examples are two-dimensional atomic structures showing the scattering and the confinement of electrons [4, 5] Using the same approach, Nilius *et al* have assembled chains of Au atoms on a NiAl(110) surface [6]. Similarly, Fölsch *et al* have manipulated individual Cu atoms to form atomic chains on the Cu(111) surface [7]. However, this approach has two inherent disadvantages for technological applications. The first one is the difficulty of fabricating a number of these atomic chains in a reasonable time and the second one is the limited temperature range at which these atomic chains remain stable.

Self-assembly is considered to be an alternative technique to the conventional lithographic techniques which slowly approach their limit of about 15 nm [8]. The biggest advantage of this method is the ease of production of the well defined, high quality structures even with rather complicated organic molecules [9, 10]. Another important advantage of self-assembly is the ability to produce structures that are stable in a rather wide temperature range. The majority of studies on self-assembled atomic chains have been performed on semiconductor surfaces, such as Pt and Au atomic chains

0953-8984/08/393001+26$30.00

on Ge(001) [11, 12], Au, Pb atomic chains on vicinal Si surfaces [13, 14] and atomic chains of Bi and rare-earth metals on Si(001) [15, 16]. This can be attributed to the technological importance of semiconductor surfaces. In addition to this, the existence of a band gap on these surfaces electronically decouples the substrate from the atomic chains and allows one to study the physics of truly one-dimensional structures.

In this topical review, the focus will be the recent experimental and theoretical studies of various one-dimensional atomic chains. Before mentioning these studies, the physics of one-dimensional structures is briefly introduced in section 2. However, interested readers are strongly encouraged to dive in to the references given in the following sections.

2. One-dimensional electron systems

2.1. Non-interacting one-dimensional electrons

The simplest model of a non-interacting electron system is an electron gas. In this model, the interactions of electrons with other electrons and with the periodic corrugations of atoms forming the crystal are neglected. This model is very simple, but it is still able to explain many properties of metals such as heat capacity, thermal conductivity, electrical conductivity, magnetic susceptibility and the electrodynamics of metals. However, in nature we do not have only metals; we have semiconductors, semi-metals and insulators. All these materials have distinctively different physical properties from metals. Therefore, it is necessary to elaborate the electron gas model in order to explain these differences. The first step is to consider the effect of the periodic corrugations of ions in the properties of the crystal. Superimposing these periodic corrugations into the electron gas model leads to formation of energy bands and allows us to explain features like the positive Hall coefficient and transport properties.

In the electron gas model, electrons are considered to be confined in a quantum box. Since this is a model for real materials, the transport properties of electrons should be addressed properly. In order to allow electron transport across the crystal, wavefunctions of electrons should satisfy periodic boundary conditions. The eigenfunctions ($\Psi_n(x)$) and eigenvalues (E_n) of the Schrödinger equation for such a one-dimensional system are given in equation (1) [17]:

$$\begin{aligned} &\Psi_n(r) = \mathrm{e}^{\mathrm{i}kx} \\ &E_n = \frac{\hbar^2}{2m}\left(\frac{n\pi}{L}\right)^2 \qquad n = 1\ldots\infty \end{aligned} \tag{1}$$

where $\hbar$ is the Planck constant, m and L are the mass of the electron and the width of the quantum well and n is a positive integer indicating the quantum number of the energy level.

The next step is to place a given number N of electrons into the energy levels properly. According to the Pauli exclusion principle, no two electrons are allowed to have identical quantum numbers. In the one-dimensional case, including spin, we have two quantum numbers, which enables us to place only two electrons (with opposite spins) in each energy level. Thus, N electrons can occupy $N/2$ states. The energy of the topmost filled level is formulated as

$$E_\mathrm{F} = \frac{\hbar^2}{2m}\left(\frac{\pi N}{2L}\right)^2. \tag{2}$$

This energy is called the Fermi energy. The definition of the Fermi energy as being the energy of the topmost filled level will keep its validity for the rest of the discussions.

Another important quantity is the density of states, which is defined as the number of possible orbitals per unit energy range. For a one-dimensional electron gas it can be derived as

$$D(E) = \frac{\mathrm{d}N}{\mathrm{d}E} \propto E^{-1/2}. \tag{3}$$

As shown in equation (3), the density of states of a one-dimensional electron gas is proportional to $E^{-1/2}$. These kinds of singularities in the density of states are called van Hove singularities, and as will be illustrated in the following section the van Hove singularity is an important indication of the existence of a one-dimensional structure [18].

It is time to include the periodic corrugations of the ions in a crystal. For the sake of simplicity, it is better to consider the problem in one dimension. The Fourier transform of the periodic potential of the ions is

$$V(x) = \sum_G V_G \cdot \mathrm{e}^{\mathrm{i}Gx} \tag{4}$$

where G is the reciprocal lattice vector and V_G are the Fourier components of the periodic potential. All the quantum states are represented by the state vectors in the Hilbert space, and all the observables are represented by Hermitian operators. The set of all eigenvectors of any Hermitian operator forms a complete basis set of the Hilbert space. In other words, it is possible to write any eigenfunctions of any Hermitian operator in terms of the eigenfunctions of another Hermitian operator [19]. By using this very fact, the eigenfunction of the new Hamiltonian can be written in terms of the eigenfunctions of the free electron gas:

$$\psi(x) = \sum_k C_k \cdot \mathrm{e}^{\mathrm{i}kx}. \tag{5}$$

So the total Hamiltonian becomes

$$\begin{aligned} &\frac{-\hbar^2}{2m}\frac{\mathrm{d}^2\psi(x)}{\mathrm{d}x^2} + V(x)\psi(x) = E\psi(x) \\ &\sum_k \frac{\hbar^2}{2m}k^2 C_k \mathrm{e}^{\mathrm{i}kx} + \sum_G\sum_k V_G C_k \mathrm{e}^{\mathrm{i}(k+G)x} \\ &= \sum_k E(k)\cdot C_k \mathrm{e}^{\mathrm{i}kx}. \end{aligned} \tag{6}$$

This equation remains valid only if all the coefficients of each Fourier component are the same. Namely,

$$\begin{aligned} &\frac{\hbar^2k^2}{2m}C_k + \sum_G V_G C_{k-G} = E(k)\cdot C_k \qquad \text{or} \\ &\left(\frac{\hbar^2k^2}{2m} - E(k)\right)\cdot C_k + \sum_G V_G C_{k-G} = 0. \end{aligned} \tag{7}$$

In the final equation, a differential equation is transformed into a set of linear equations. In order to find the exact solution of this equation, it is necessary to consider an infinite number of linear equations. Taking into account only the first few of these linear equations is a good approximation if the Fourier expansion of the periodic potential converges rapidly. For any given k value, the solutions of these equations, $E(k)$, forms the set of energy values, in other words the possible band energies.

Now, consider a crystal containing N primitive cells, each with length a, which means the size of the crystal is $L = Na$. Since we have a finite size crystal, unlike equation (1), the possible k values are the integers bounded between $\pm N$:

$$k = 0; \pm\frac{2\pi}{L}; \pm\frac{4\pi}{L}; \ldots; \frac{N\pi}{L}. \tag{8}$$

Since $\frac{N\pi}{L} = \frac{\pi}{a}$, the number of independent k points in the Brillouin zone is determined by the number of primitive cells in the crystal. For N primitive cells, there are N linear equations as shown in equations (6) which can be solved to find all possible energy values. So the total number of energies becomes N. Including spin we have $2N$ possible orbitals in which to place electrons. Depending on the number of atoms and electrons in a primitive cell, the bands can be filled partially or completely. The crystals with completely filled bands are called insulators, whereas the crystals with partially filled bands are called metals [20].

2.2. One-dimensional interacting electron systems

Up to now, we have neglected the interaction between electrons; now it is time to include them in the model. The derivations and equations given in this section and in the following section are mainly a brief and simplified summary. Interested readers are referred to the relevant books and reviews referenced in this section.

The first obvious method is to consider the inhomogeneous part of the electron–electron interactions as a perturbation to the non-interacting electrons in the jellium model [21]. The homogeneous part is $q = 0$, and from now on in all summations $q = 0$ is not included.

In this model, the ion–ion, the electron–ion and the electron–electron interactions are considered to cancel each other, and the periodic corrugations of the ions are replaced by a constant positive charge density. The only remaining term in the Hamiltonian, as in the free electron gas model, is the kinetic energy term. The result of the first-order perturbation theory shows that the three-dimensional free electron gas is stable in the presence of the Coulomb interaction:

$$\frac{E}{N} = \frac{E^0 + E^1}{N} = \left(\frac{3\hbar^2 k_F^2}{10m} - \frac{e^2 V k_F^4}{4N\pi^3}\right). \tag{9}$$

However, the second-order perturbation diverges, indicating that it is not possible to improve accuracy of the calculations by considering higher-order terms in the perturbation.

This may appear to be a difficult problem. However, there is a way to overcome this difficulty. Consider an electron traveling in a crystal: due to the mutual interactions between this electron and its surroundings, the electron constantly creates a disturbance around itself. This disturbance moves together with the electron. The disturbance together with the particle itself is called a quasi-particle [22]. The model based on this quasi-particle picture is known as the Fermi liquid theory. The validity of the quasi-particle picture relies on adiabatic continuity, i.e. the excitations of the non-interacting system and interacting system should be correlated in such a way that when the excitations are slowly turned on, the occupation number of the states of the non-interacting system should remain unchanged.

The Hartree–Fock model is the simplest model for interacting electrons. In this model, only the forward and the exchange scatterings are considered. In forward scattering, there is no change in the momentum of the particles upon scattering. However, in exchange scattering, each time the particles are scattered, instantaneously, an electron–hole pair is created and annihilated. Using Coulomb interactions it is possible to calculate the energy of the quasi-particle:

$$E'_k = \frac{k^2}{2m} - \frac{e^2 k_F}{2\pi}\left[2 + \frac{(k_F^2 - k^2)}{k k_F}\ln\left|\frac{k + k_F}{k - k_F}\right|\right]. \tag{10}$$

Since effective mass is defined as

$$m = k_F \bigg/ \left(\frac{dE'_F}{dk}\right)_{k_F}, \tag{11}$$

using equations (10) and (11) it can be shown that the effective mass, m, around the Fermi level becomes zero. A replacement of the Coulomb potential with the screened Coulomb potential (also known as the Yukawa potential) would be enough to get rid of this awkward result. This replacement also helps to tackle the divergent integrals that emerge in the further calculations. However, even replacing the Yukawa potential does not remove the conceptual deficiency originating from the Hartree–Fock model. The problem can be shown easily on the Feynman diagrams shown in figure 1 (see [22] for details).

As indicated in figure 1, at any time t (dashed line) we have only a bare particle. However, we know that the quasi-particle is nothing but a bare particle surrounded by an interaction cloud and the importance of the interaction cloud increases when the density of the particle becomes larger. The absence of the time-dependent interaction cloud makes the Hartree–Fock model insufficient to describe the densely populated electron sea.

The solution to this problem comes when we include some of the perturbation terms omitted in the Hartree–Fock model. This new approximation is called the ‘random phase approximation’ or simply RPA Feynman diagrams of the RPA approximation are shown in figure 2 (see [22] for details).

The difference comes from the diagrams showing the ‘effective interactions’. The term ‘effective interactions’ refers to the existence of indirect interactions between two electrons via the many-body system. Another key point in these diagrams is the existence of holes and electrons at the same time for certain time intervals. Actually, in this way the medium becomes ‘polarized’ [23].

The susceptibility $\chi(q, w)$ measures the response of the electron gas to an external potential and it is defined as

$$\chi(q, \omega) = \frac{1}{L^d}\sum_k \frac{f_F(E_k) - f_F(E_{k+q})}{\omega + E(k) - E(k+q) + i\delta}. \tag{12}$$

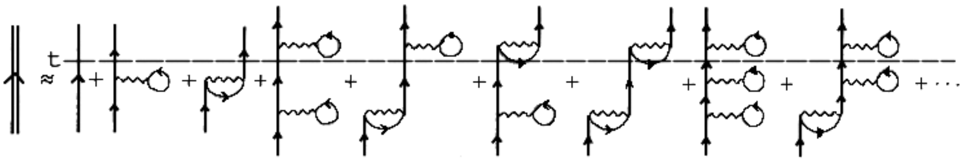

Figure 1. Feynman diagram of the Hartree–Fock model. In the figure bubble diagrams represent forward scattering and open oyster diagrams represent exchange scattering, and both of these scattering events are instantaneous.

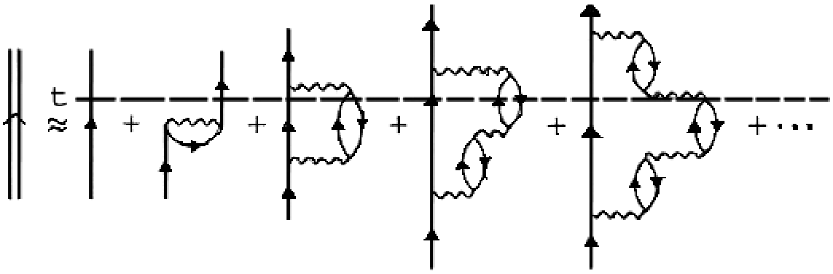

Figure 2. Feynman diagrams of RPA approximation. The diagram in the third term is called a ring diagram, showing the creation of a particle–hole pair and at a later time the annihilation of this particle–hole pair. At any given time the particle is accompanied by particle–hole pairs.

The energy, $E(k)$ is measured relative to the Fermi level, therefore when k is on the Fermi level, $E(k) = 0$. This might lead to singularities when $\omega = 0$, (static susceptibility). A singularity is possible if $E(k+q)$ is zero for $q \neq 0$. In two- and three-dimensional systems there are only very limited numbers of these kinds of q vectors. Since there is a summation over all k points, these singularities are smoothed out. The singularities remain only in the derivative of $\chi(q, \omega = 0)$. The singularities in the derivative of $\chi(q, \omega = 0)$ are the origin of Friedel oscillations [24, 25]. The singularity in $\chi(q, \omega = 0)$ exists only if there is a finite size domain of k values satisfying the condition given below:

$$E(k + q) = E(k).$$

This is called nesting. In a one-dimensional system, there is always a vector, $q = 2k_F$, creating the singularity independent from the dispersion relation (see figure 4). The existence of a singularity means that there is no adiabatic continuity. Thus the very basic assumption of Fermi liquid theory stating that starting from the non-interacting system of particles it is possible to reach the interacting case by applying perturbation theory fails in one dimension. Thus, a new model explaining the properties of the interacting one-dimensional electron gas is necessary.

The dispersion relation of excitations in a three-dimensional system and a one-dimensional system is quite different. In a three-dimensional system, the electron–hole and plasmon excitations are clearly separated. Therefore, plasmon excitations are stable and cannot decay through emitting electron–hole pairs. On the other hand, the low energy excitations in a one-dimensional system are plasmons and they are possible in a narrow band for q values very close to zero (forward scattering) and $2k_F$ (backward scattering). This very fact will be used when forming the Luttinger–Tomonaga model. We consider the impossibility of individual movement of any electron in a one-dimensional interacting system.

2.3. The Luttinger–Tomonaga model

The failure of Fermi liquid theory to explain one-dimensional interacting electrons led to the development of a new model, called the Luttinger–Tomonaga model [3, 26, 27]. In this model, the excitations of the one-dimensional system are defined as particles moving to the right and left. The validity of this assumption relies on the fact that the excitation energies are small compared to the Fermi energy. The Hamiltonian of the interacting electrons can be defined as [28]

$$\begin{aligned} H &= H_0 + H_{\text{int}} \\ H_0 &= \sum_k \varepsilon_k c_k^\dagger c_k \\ H_{\text{int}} &= \frac{1}{2L} \sum_{kk'q} V(q) c_k^\dagger c_{k'}^\dagger c_{k'-q} c_{k+q} \end{aligned} \qquad (13)$$

where c_k and $c_k^\dagger$ are the annihilation and creation operators for Fermions with a wavevector k, ε_k is the eigenvalue of the non-interacting Hamiltonian and $V(q)$ is the Fourier transform of the repulsive interaction between electrons.

The crucial approximation in the Luttinger–Tomonaga model is to assume a linear dispersion relation:

$$\varepsilon_k \approx (|k| - k_F)\upsilon_F.$$

In the Tomonaga model, linear dispersion is assumed to be valid in a limited energy window; however, in the Luttinger model linear dispersion is assumed to be valid for all real values of k and the fermions with opposite k vectors are assumed as two different species.

Now, it is possible to rewrite the electron creation and annihilation operators as a function of the creation and

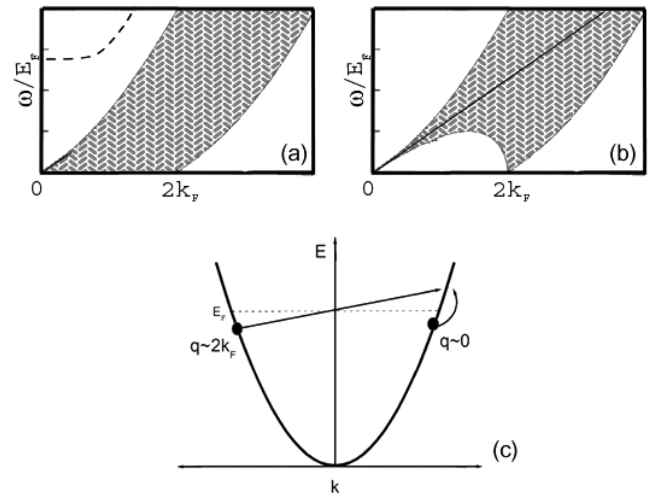

Figure 3. (a), (b) Particle–hole spectrum of a three-dimensional and a one-dimensional systems, respectively. The dashed line in (a) shows the plasmon dispersion in the three-dimensional system. The solid line in (b) shows the plasmon dispersion in the one-dimensional system. (c) The two low energy excitations in a one-dimensional system.

annihilation operators of left- and right-moving electrons:

$$\begin{aligned} c_k &= c_{k\mathrm{R}}\Theta(k) + c_{k\mathrm{L}}\Theta(-k) \\ c_k^\dagger &= c_{k\mathrm{R}}^\dagger\Theta(k) + c_{k\mathrm{L}}^\dagger\Theta(-k). \end{aligned} \tag{14}$$

Since the left- and right-moving particles are considered as different, it is possible to assign new density operators for them, $\rho_\mathrm{R}(q)$ and $\rho_\mathrm{L}(q)$:

$$\begin{aligned} \rho_\mathrm{R}(q) &= \sum_{k>0} c_{k\mathrm{R}}^\dagger c_{k+q\mathrm{R}} \\ \rho_\mathrm{L}(q) &= \sum_{k<0} c_{k\mathrm{L}}^\dagger c_{k+q\mathrm{L}}. \end{aligned} \tag{15}$$

By calculating commutation relations between left- and right-moving density operators we can prove that they behave like bosons:

$$\begin{aligned} [\rho_\mathrm{R}(q), \rho_\mathrm{R}(-q')] &= \delta_{qq'}\frac{q\zeta}{2\pi} \\ [\rho_\mathrm{L}(q), \rho_\mathrm{L}(-q')] &= -\delta_{qq'}\frac{q\zeta}{2\pi} \\ [\rho_\mathrm{R}(q), \rho_\mathrm{L}(-q')] &= 0. \end{aligned} \tag{16}$$

In terms of these density operators, H_0 becomes

$$\begin{aligned} H_0 = \frac{2\pi\upsilon_\mathrm{F}}{L}\sum_{q>0}[\rho_\mathrm{R}(-q)\rho_\mathrm{R}(q) \\ + \rho_\mathrm{L}(q)\rho_\mathrm{L}(-q)] + C(N_\mathrm{R}, N_\mathrm{L}) \end{aligned} \tag{17}$$

where $C(N_\mathrm{R}, N_\mathrm{L})$ is constant and depends on the number of particles.

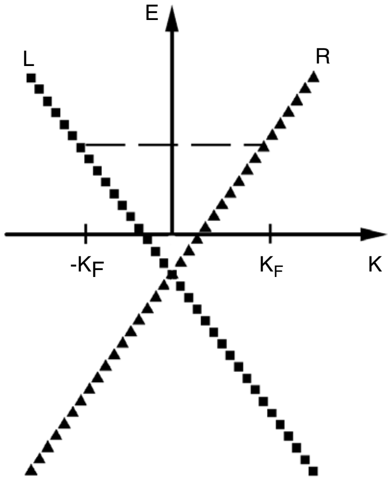

Figure 4. The linear dispersion relation of the one-dimensional electron system. The letters L and R indicate branches of left- and right-moving electrons, respectively.

As indicated in figure 3, there are two possible scattering geometries[1]. The first one, forward scattering, occurs when both particles are on the same side of the Fermi surface ($q \approx 0$). The other one, backscattering, defines the scattering of particles located on the opposite sides of the Fermi surface $q \approx 2k_\mathrm{F}$. By using the density operators given above, it is possible to write down

$$\begin{aligned} H_\mathrm{int} = \frac{1}{L}\sum_{q\neq 0} V_1(q)\cdot\left[\rho_\mathrm{R}(q)\rho_\mathrm{R}(-q) + \rho_\mathrm{L}(q)\rho_\mathrm{L}(-q)\right] \\ + \frac{1}{L}\sum_{q\neq 0} V_2(q)\cdot\left[\rho_\mathrm{R}(-q)\rho_\mathrm{L}(q) + \rho_\mathrm{L}(-q)\rho_\mathrm{R}(q)\right]. \end{aligned} \tag{18}$$

Based on these operators it is possible to define the following boson operators:

$$\begin{aligned} b_q &= \sqrt{\frac{2\pi}{|q|\,L}}(\Theta(q)\rho_\mathrm{R}(q) + \Theta(-q)\rho_\mathrm{L}(q)) \\ b_q^\dagger &= \sqrt{\frac{2\pi}{|q|\,L}}(\Theta(q)\rho_\mathrm{R}^\dagger(q) + \Theta(-q)\rho_\mathrm{L}^\dagger(q)). \end{aligned} \tag{19}$$

So the total Hamiltonian can be defined in terms of these bosonic operators

$$H = H_0 + H_\mathrm{int}$$

$$\begin{aligned} H = \upsilon_\mathrm{F}\sum_{q\neq 0}|q|\,b_q^\dagger b_q + \frac{1}{2\pi}\sum_{q\neq 0}|q|\,V_1(q)b_q^\dagger b_q \\ + \frac{1}{4\pi}\sum_{q\neq 0}|q|\,V_2(q)(b_q^\dagger b_{-q}^\dagger + b_{-q}b_q). \end{aligned} \tag{20}$$

Diagonalizing the Hamiltonian gives the eigenvalues of these bosonic excitations

$$H|q\rangle = E_q|q\rangle = q\sqrt{\left|\upsilon_\mathrm{F} + \frac{V_1(q)}{2\pi}\right|^2 - \left|\frac{V_2(q)}{2\pi}\right|^2}. \tag{21}$$

Up to this point the existence of spin was neglected, and it is found that one-dimensional interacting charged particles create bosonic charge density waves. Addition of the spin

---

[1] Actually there is a third one called the umklapp process which is important only when the band is close to half full.

degree of freedom in the derivations above shows that the spin and charge parts of the Hamiltonian are independent. Commutation relations for the new charge and spin operators follow bosonic rules. Starting from equation (18) we can derive the Hamiltonian:

$$H_{\mathrm{int}} = \frac{1}{L}\sum_{q\neq 0} V_1(q)\cdot\left[\rho_{\mathrm{R}}(q)+\rho_{\mathrm{L}}(q)\right]\left[\rho_{\mathrm{R}}(-q)+\rho_{\mathrm{L}}(-q)\right] + \frac{1}{L}\sum_{q\neq 0,\sigma}(V_2(q)-V_1(q))\cdot[\rho_{R,\sigma}(-q)\rho_{L,\sigma}(q) + \rho_{L,\sigma}(-q)\rho_{R,\sigma}(q)]. \tag{22}$$

The second part of the summation with the interaction term, $V_2(q) - V_1(q)$, deals with the backscattering, and it is possible only if the spin of the particles are parallel. Scattering of particles with unparallel spin leads to spin flipping, and spin flipping cannot be expressed in bosonic form.

The total Hamiltonian is exactly the same as equation (20) except now each boson operator has spin indices:

$$H = \upsilon_{\mathrm{F}}\sum_{\substack{q\neq 0\\ \sigma}}|q|b^{\dagger}_{q,\sigma}b_{q,\sigma} + \frac{1}{2\pi}\sum_{\substack{q\neq 0\\ \sigma\sigma'}}|q|V_1(q)b^{\dagger}_{q,\sigma}b_{q,\sigma'} + \frac{1}{4\pi}\sum_{\substack{q\neq 0\\ \sigma}}|q|V_2(q)(b^{\dagger}_{q,\sigma}b^{\dagger}_{-q,\sigma} + b_{-q,\sigma}b_{q,\sigma}). \tag{23}$$

In order to uncouple the spin-up and-down operators, spin-symmetric and spin-antisymmetric operators are defined as

$$b_q^C = \frac{1}{\sqrt{2}}(b_{q,\uparrow} + b_{q,\uparrow}) \qquad \text{and} \qquad b_q^S = \frac{1}{\sqrt{2}}(b_{q,\uparrow} - b_{q,\uparrow}). \tag{24}$$

These new operators allows the division of the total Hamiltonian into two pieces

$$H = H_C + H_S$$

$$H_C = \sum_{q\neq 0}\left(\upsilon_{\mathrm{F}} + \frac{V_1(q)}{\pi}\right)|q|b_q^{C+}b_q^C + \frac{V_1(q)+V_2(q)}{4\pi}|q|(b_q^{C+}b_{-q}^{C+} + b_{-q}^C b_q^C) \tag{25}$$

$$H_S = \sum_{q\neq 0}\upsilon_{\mathrm{F}}|q|b_q^{S+}b_q^S + \frac{V_2(q)+V_1(q)}{4\pi}|q| \times (b_q^{S+}b_{-q}^{S+} + b_{-q}^S b_q^S).$$

Using Bogoliubov transformation it is possible to diagonalize the Hamiltonian. Each piece of the Hamiltonian defines two independent excitations, i.e. spin (H_S) and charge (H_C).

The eigenvalues of these two independent excitations are given by

$$\upsilon_q^C = \sqrt{\left(\upsilon_{\mathrm{F}} + \frac{V_1(q)}{\pi}\right)^2 - \left(\frac{V_1(q)+V_2(q)}{2\pi}\right)^2}$$

$$\upsilon_q^S = \sqrt{\upsilon_{\mathrm{F}}^2 - \left(\frac{V_1(q)+V_2(q)}{2\pi}\right)^2}.$$

Even though we reach the point where we can calculate the eigenvalues of the individual excitations of one-dimensional interacting particles, we still need to develop a formalism which we can correlate with the real experimental result. In order to learn the electronic properties of systems, various spectroscopic methods are used. In the examples that we will discuss in the following sections, mainly scanning tunneling spectroscopy (STS) and photoemission spectroscopy are employed. Both of these techniques are used to measure the density of states. This brings us to the point at which we can speculate on the density of states of the one-dimensional interacting systems.

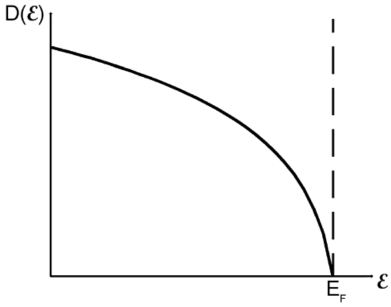

Figure 5. The density of states of one-dimensional interacting particles. The density of states goes to zero following a power law, indicating that there is no state showing single-particle excitation properties at the Fermi level.

$A(\upsilon, w)$ is called the spectral function and it can be considered as the projection of the spectral density at energy w on to the state υ:

$$A(\upsilon, w) = -2\,\mathrm{Im}\,G_{\mathrm{R}}(\upsilon, w)$$

where $G_{\mathrm{R}}(\upsilon, w)$ is the retarded Green's function which defines, in the frequency domain, the propagation of a particle in state υ.

The density of states can be formulated as

$$D(\omega) = \sum_{\upsilon} A(\upsilon, w) \propto |\varepsilon|^{\frac{1}{2}\cdot[K+K^{-1}]-1}.$$

Here K is a function of interaction of the coupling constants of two scattering events. Generally speaking if $K < 1$ then the interaction between particles is repulsive leading to the charge density waves. If $K > 1$ then the interaction between the particles becomes attractive, which leads to superconducting fluctuations.

In STM tunneling current can be defined as

$$I(V) = \int_{-\infty}^{\infty}\frac{\mathrm{d}\omega}{2\pi}\sum_{\upsilon,\mu}|T_{\upsilon\mu}|^2 A_1(\upsilon,\omega)A_2(\mu,\omega+eV) \times (f(\omega+eV) - f(\omega)).$$

It is easy to follow the equation for current given above. The transmission term, $T_{\upsilon\mu}$, takes the quality of coupling, summation over spectral functions, A_1, A_2, defines the density of states of the Luttinger liquid and metal scanning tunneling microscope tip and the availability of the states is given by the difference in the occupation functions. The density of states of a metal around the Fermi level can be assumed as constant. The tunneling transmission matrix can be also assumed constant at low biases. These two approximations lead to the simplification in the tunneling current formalism defined above:

$$I(V) \propto \int_{-\infty}^{\infty} \frac{\mathrm{d}\omega}{2\pi} \sum_{\upsilon} A_1(\upsilon, \omega)(f(\omega + eV) - f(\omega)).$$

So the derivative of the tunneling current, which is proportional to the density of states is given as

$$\frac{\mathrm{d}I(V)}{\mathrm{d}V} \propto \int_{-\infty}^{\infty} \frac{\mathrm{d}\omega}{2\pi}(f(\omega + eV) - f(\omega)) \sum_{\upsilon} A_1(\upsilon, \omega)$$

$$\frac{\mathrm{d}I(V)}{\mathrm{d}V} \propto \sum_{\upsilon} A_1(\upsilon, -eV).$$

Based on the discussions above, the STS was successfully used to determine the Luttinger liquid behavior of carbon nanotubes [29].

Peierls instability

In his book 'Quantum theory of solids' Peierls explains the effect of a periodic distortion on the physical properties of linear chains [30]. The idea is based on the fact that any periodic lattice distortion redefines the size of the unit cell. In other words, if the periodic lattice distortions repeat themselves every nth atom, then the size of the unit cell in reciprocal space shrinks to $\frac{1}{n}$th of the original one. This reduction in the size of the unit cell leads to the splitting of each band in the original unit cell into n new bands. The maximum gain in energy is obtained if $n = 2$. In this case, including spin, each atom has only one electron, namely the one-dimensional band is half filled. In an ideal one-dimensional system, the Peierls transition occurs at $T = 0$ K, whereas, in reality, one-dimensional systems couple with the substrate and/or with each other. Such a system loses its ideal one-dimensionality and undergoes a Peierls instability at a temperature above 0 K. This phenomenon, as discussed in the following sections, has significant influence on the electronic properties of the atomic chains at low temperatures.

3. Recent studies of various atomic chains formed on surfaces

Due to the vast number of studies related to atomic chains, only selected, but subjectively remarkable, studies are presented in the following sections. These studies can be divided into two main groups based on the way the atomic chains are manufactured. The first group focuses on artificially formed atomic chains. These chains are formed with the help of the scanning tunneling microscope. Due to their limited size and coverage, the experimental studies of these atomic chains are restricted to scanning probe techniques. The second group focuses on self-assembled atomic chains. The length of these chains, depending on the substrate and the atoms forming the chain, can reach hundreds of nanometers. The relatively large scale of the atomic chains increases the number of applicable techniques, ranging from scanning probe to photoemission based techniques.

3.1. Artificially formed atomic chains

STM does not only provide images with sub-nanometer resolution, it can also be employed as a manufacturing tool in the nano-world. Artificial, human-made structures on the surfaces are rather convenient substrates for measuring the quite unusual physical and chemical properties of these low-dimensional systems. The main purpose of these experiments was to study the effect of coupling between individual atoms and between the atoms of the chain and the substrate on the electronic properties of the individual atoms.

3.2. Au atomic chains on NiAl(110)

The pioneering work on the physical properties of artificial atomic chains was the study of Au atomic chains formed on the NiAl(110) surface [31]. In this work the resistance between the STM tip and the sample was lowered so that a small attractive force between the individual atoms on the surface and the tip apex was formed. Using this small force, the atoms were pulled to predetermined adsorption sites (in this case on top of Ni atoms) and used to assemble atomic chains of various lengths.

STS measurements performed on a single Au atom show a distinctive peak located at 1.95 V. Placing another Au atom on the neighboring site leads to the formation of a dimer. As in the formation of the hydrogen molecule, the peak assigned to the Au adatom splits into two and forms peaks located at 1.5 and 2.25 V. Further increase in the number of atoms in the atomic chain pushes the lowest state towards the Fermi level. For a Au chain of 20 atoms, the state with lowest energy is located at 0.75 V. (See figure 7(c).)

Figure 6(a) shows the $\mathrm{d}I/\mathrm{d}V$ measurements taken on top of a chain containing 20 Au atoms. Due to the finite peak width and the dominant lowest energy state, it is not possible to resolve the position of each state in the spectrum. The $\mathrm{d}I/\mathrm{d}V$ mappings of the atomic chains measured at various sample biases show density fluctuations resembling the eigenstates of a one-dimensional quantum well (see figure 6(c)). However, due to the finite peak width, these measured $\mathrm{d}I/\mathrm{d}V$ maps are not the eigenstates but they are the superposition of a few eigenstates with adjacent eigenvalues. The weight of each eigenstate is determined by the coefficients, and the coefficients are extracted from the fitting of the $\mathrm{d}I/\mathrm{d}V$ pattern to the squared wavefunctions. The maximum value of each coefficient determines the position of the corresponding state (see figure 7(a)). From the fitting of the position of these states with the theoretical dispersion relation, $E(k) = E_0 + \frac{\hbar^2 k^2}{2m_e}$, the onset energy, E_0, and the effective mass, m_e, of the electron is found—0.68 eV and 0.5 m_0, respectively (m_0 is the free electron mass). As predicted, the energy dependence of the conductivity for a Au_{20} chain (dashed line) matches the calculated DOS of a one-dimensional free electron gas (dotted line) and a 60 Å long quantum well (solid line). This result supports the claim for the existence of one-dimensional electron system and the sufficiency of a one-dimensional quantum well as a physical model for this system (see figure 7(d)).

Another prediction of the one-dimensional quantum well model is that the position of the ground state is inversely

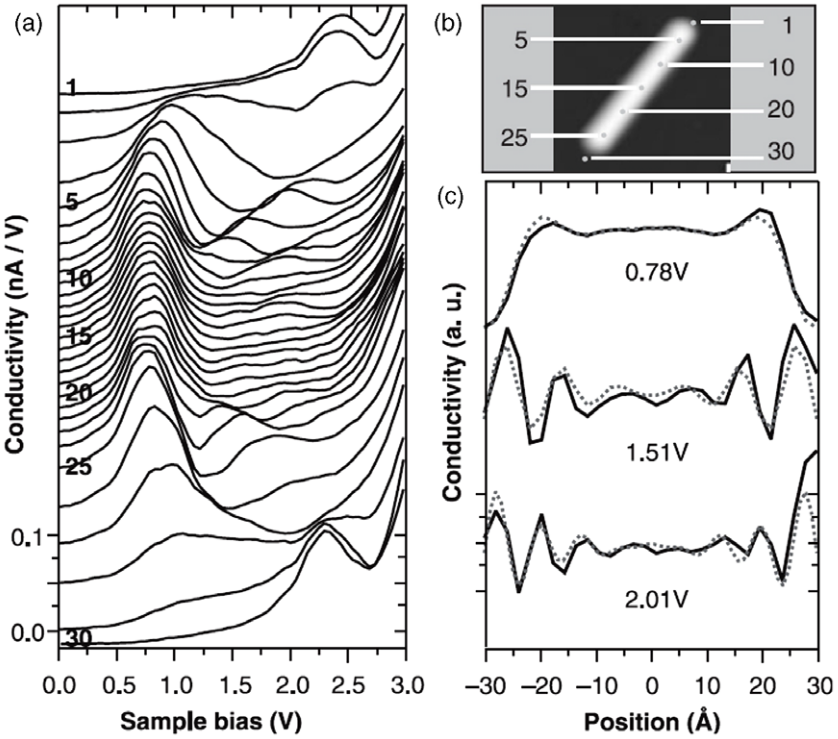

Figure 6. (a) Conductivity (dI/dV) spectra measured along Au_{20}. The sample bias is 2.5 V and the tunneling current is 1 nA. (b) The positions where the spectra were measured are marked in the topographic image of Au_{20}. (c) Vertical cuts through dI/dV spectra shown in (a) at three exemplary energies. Conductivity patterns are fitted with the sum of squared sinusoids of fixed wavevector $\frac{\pi n}{L}$ and adjustable weight c_n (dotted curves). The coefficients extracted from the fitting are $c_1 = 0.31$, $c_2 = 0.29$, $c_3 = 0.26$, $c_4 = 0.11$, for 0.78 V; $c_5 = 0.26$, $c_6 = 0.5$, $c_7 = 0.24$, for 1.51; and $c_6 = 0.13$, $c_7 = 0.29$, $c_8 = 0.39$, $c_9 = 0.19$ for 2.01. Reproduced with permission from [31]. Copyright 2002 from AAAS.

proportional to the square of the width of the well. The experiments performed on Au chains of various widths show that the position of the lowest state is inversely proportional to the length of the chain, indicating that the initial claim to model the system as a one-dimensional quantum well is correct.

Apparently, there must be a reason why the one-dimensional quantum well is sufficient to describe the electronic properties of the atomic chain. Density functional theory (DFT) calculations on the Au atomic chains show that the origin of the states comes from the 6s and 6p states. In an isolated Au atom, these states are located at −1.2 and 3.9 V. However, due to the interaction with the substrate the 6s state splits into two and intermixes with the down-shifted 6p orbital. The unoccupied state is located at 1.75 eV. Due to the Stark effect induced by the STM tip, this state shifts to 1.91 eV, which is close to the observed value of 1.95 eV. The formation of dimers leads to the splitting of this state. For free dimers, the amount of splitting is inversely proportional to the separation of the Au atoms. In order to study the effect of the substrate on the width of the splitting, researchers have performed STS experiments on various dimer configurations with different separations and they have compared these experimental results with the calculations of free and NiAl-supported Au dimers. The experimental results indicate that the splitting in the states of dimer I is small compared to the calculated splitting in the states of a free dimer I. This result shows that NiAl(110) substrate screens the direct orbital interaction and reduces the width of the splitting. On the other hand, the splitting in the state of dimer IV is large than the calculated splitting in the state of a free dimer IV, indicating that the NiAl(110) surface initiates a coupling between two Au atoms. Based on these experimental results we can safely conclude that the states of individual Au atoms couple through the NiAl(110) substrate and depending on the distance between individual Au atoms, the substrate may decrease or increase the coupling between these atoms [32].

3.3. *Pd atomic chains on NiAl(110)*

Experiments similar to those presented in section 3.2 were performed with Pd atoms in order to study the effect of chemical composition of the atoms on the electronic properties of the chains [33]. STS measurements show that the individual Pd atom positioned on the NiAl(110) substrate creates a peak located at 2.8 V in the tunneling spectra. Dimerization leads to the splitting of this peak into two peaks located at 2.05 and 2.55 V. The peak located at 2.05 V moves towards the Fermi level when the length of the atomic chain increases. Similar to Au chains, the position of the lowest state is inversely proportional to the square of the length of the atomic chains, suggesting the possibility of using a one-dimensional quantum well model (see figure 10(c)). dI/dV maps measured along the atomic chain of 20 Pd atoms show density fluctuations similar to the ones measured on Au chains (see figure 9).

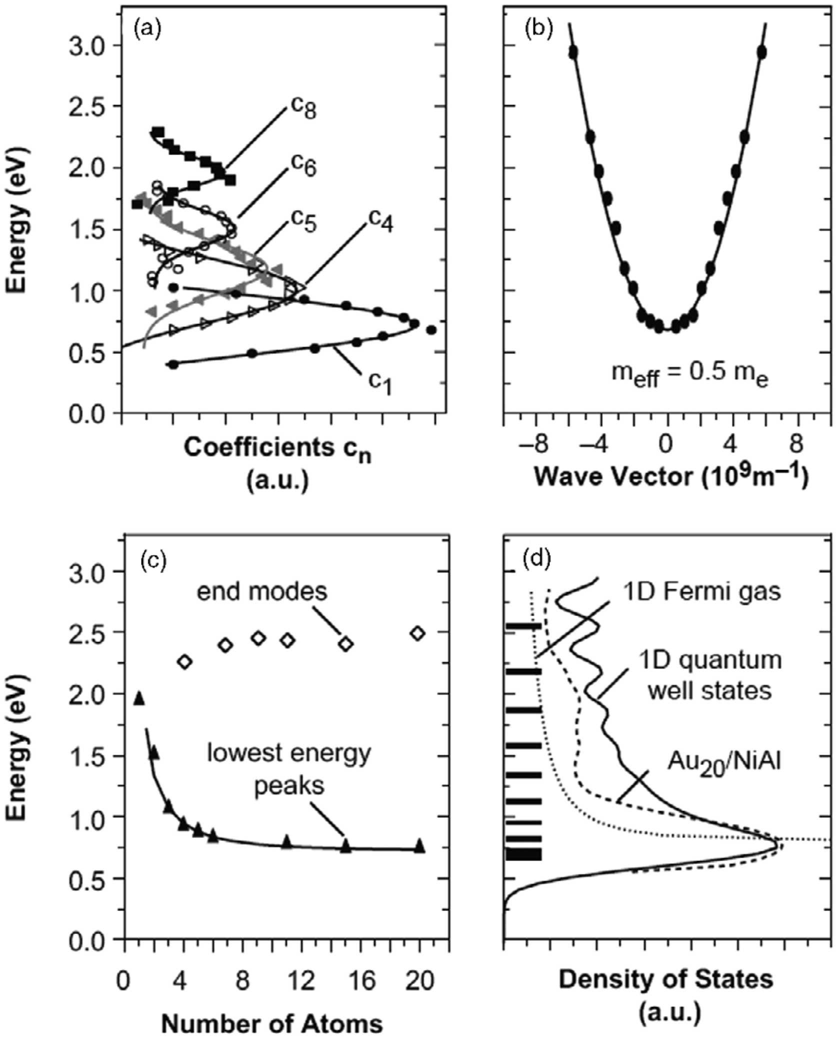

Figure 7. (a) Selected coefficients c_n obtained from the fitting procedure of conductivity patterns along a Au_{20} chain. The maximum for each c_n identifies the energy of the eigenstate with wavevector $k = \pi n/L$. (b) Dispersion relation of electronic states for a Au_{20} chain, with each point (E, k) obtained from (a). (c) Lowest energy conductivity peaks and end modes for Au chains with an increasing number of atoms. The lowest energy peaks for Au_3–Au_{20} are fitted with an L^2 dependence on chain length L (solid lines). (d) Energy dependence of the conductivity for a Au_{20} chain (dashed line) in comparison to the calculated DOS for a 60 Å long quantum well (solid line) and a one-dimensional free electron gas (dotted line). Quantum well states are marked with bars along the left axis. Reproduced with permission from [31]. Copyright 2002 from AAAS.

The ground state of the atomic chain of 20 Pd is at 1.51, which is significantly higher than the ground state of the Au chain of the same length. The fitting of squares of the sinusoidal wavefunctions of the one-dimensional quantum well allows determination of the location of individual states in the spectrum (see figures 10(a) and (d)). From the fitting, the onset energy, E_0, of 1.5 eV and effective mass, m_e, of $0.65 \cdot m_0$ was extracted (see figure 10(b)). The onset energy and the effective mass values are significantly different from the ones measured for the Au chain. The difference in the onset energy is attributed to the lower coupling between individual Pd adatoms and the coupling of these atoms with the NiAl(110) surface. Intuitively, the decrease in the coupling between Pd atoms is attributed to the relatively smaller 5sp orbital of Pd atoms compared to the 6sp orbital of Au atoms. This relatively small coupling of Pd atoms also explains the higher effective electron mass measured on Pd atomic chains. In bulk, the larger confinement of Pd orbitals leads to a smaller lattice constant (2.75 Å) compared to the lattice constant of Au (2.89 Å). The difference in lattice constants due to confinement of Pd orbitals may seem quite small, but it is still significantly large considering the fact that the coupling between the individual atoms is due to the exponentially decaying electronic states of atoms. Another remarkable difference between Pd and Au is the difference in the filling of the d orbital. However, because of the more localized nature of the d orbitals, these orbitals are less effective in the binding, and therefore they do not have any apparent role.

3.4. Impurity atoms on atomic chains

It is worth noting here the studies of the effect of the impurity atoms in the electronic properties of the atomic chains. Pd impurities in Au chains and Co impurities in Cu chains are

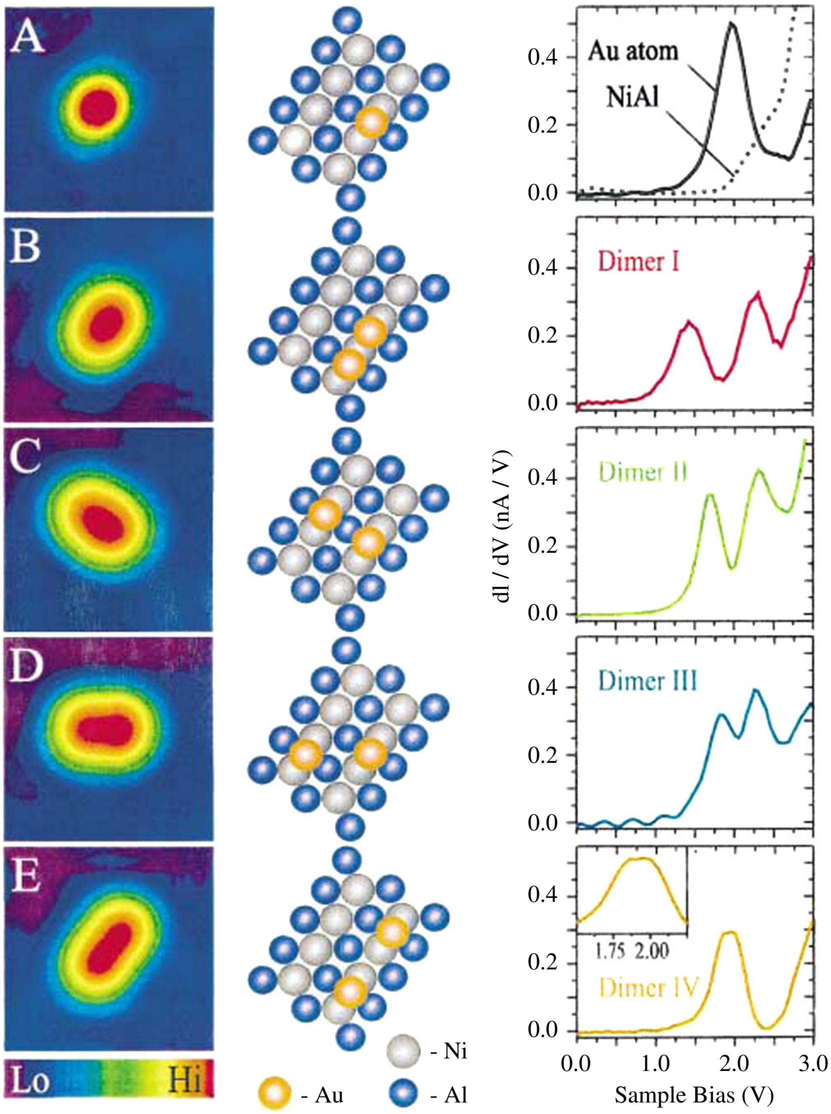

Figure 8. (a)–(e) Topographic images (size 25 Å × 25 Å. Sample bias is 2 V. The tunneling current is 0.1 nA), structure models, and $\mathrm{d}I/\mathrm{d}V$ spectra for a Au atom and different Au dimers on NiAl(110). While measuring $\mathrm{d}I/\mathrm{d}V$ spectra the sample bias was set at 2 V. The tunneling current was 0.1 nA. Reproduced with permission from [32]. Copyright 2003 by the American Physical Society.

two key examples showing rather different effects on the host atomic chains.

As in connection with the previous sections, it is better to start with the Pd atoms in the Au chains. Both an individual Pd atom and a dimer of Pd atoms were used as impurities in Au chains [34]. As previously mentioned, Au and Pd chains were studied on top of Ni atoms on a NiAl(110) surface. STS measurements performed on individual Au and Pd atoms show the characteristic peaks located at 2 eV and 2.90 eV, respectively. A dimer formed from Au and Pd atoms show two peaks at 1.7 and 2.75 eV; both of them are shifted down from the peaks of individual Au (2 eV) and Pd (2.90 eV) atoms. Further addition of Au atoms shifts the lower peak downward. However, when two Au atoms were placed on each side of the Pd atom, a peak suddenly emerges at 2.15 V and the position of this peak does not shift upon the addition of extra Au atoms to the chain. Similarly, in Au chains with a Pd dimer as an impurity, localized impurity states emerge abruptly at 2.25 and 2.95 eV when the chain has Au_2Pd_2Au, and the further addition of Au atoms does not change the energy level of these states. $\mathrm{d}I/\mathrm{d}V$ maps measured on Au_5PdAu_4 chains show that Pd atom acts like a barrier and separates two Au chains (see figure 12). Each chain can be modeled as an independent one-dimensional quantum well.

A similar study was performed on the atomic chains of Cu decorated with Co impurities [35]. A constant current image measured with STM contains information about both topography and chemical composition. The constant current images of the Co adatom and the Co atoms attached to the Cu chain appear higher than the Cu atoms on the Cu(111) surface, which allows one to distinguish the Cu and the Co atoms on the surface. Using the STM tip as a manipulator, atomic chains of various Co–Cu combinations were built. The effect of Co impurities on the electronic structure of the Cu atomic chains was studied with STS measurements (see

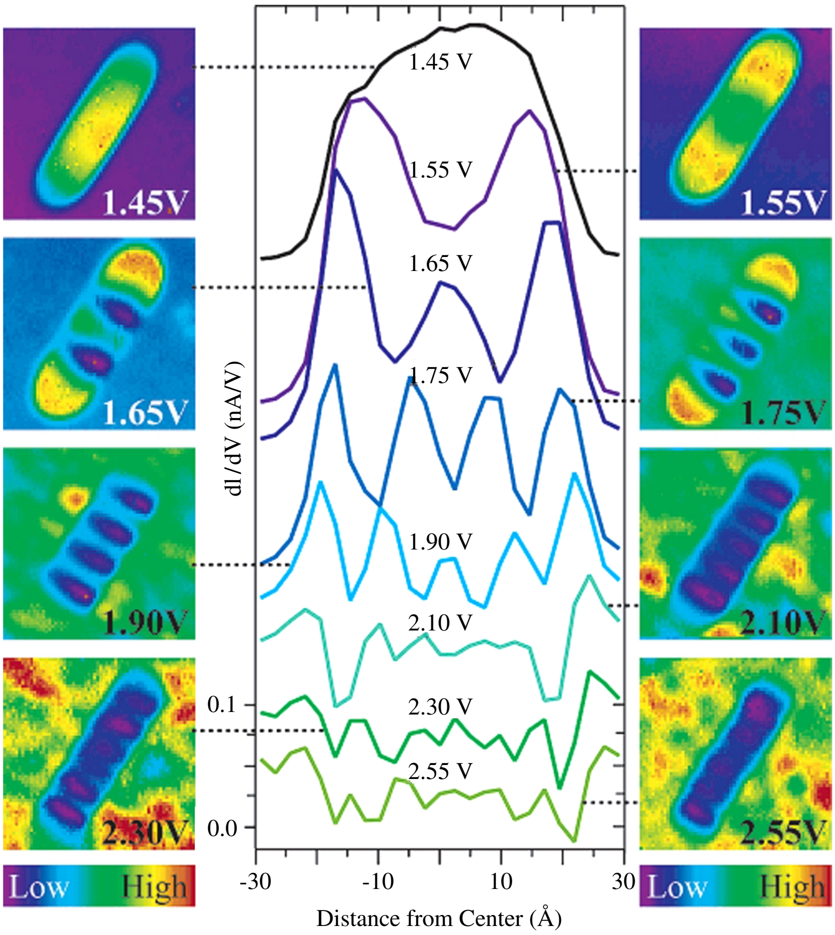

Figure 9. Cuts through the dI/dV spectra and conductance images of a Pd_{20} chain on NiAl(110), taken at $I = 1.0$ nA and the indicated sample bias. Each image is 65 Å × 65 Å. Both techniques reveal a similar number of dI/dV oscillations along the chain axis, which increases with increasing sample bias. Reprinted with permission from [33]. Copyright 2005 American Chemical Society.

figure 13). One major effect of the existing Co impurities is the downshift of the energy of the quantum states of the atomic chain. Figure 13(g) shows the trend in the shift of the ground state and the first excited state of the Co–Cu atomic chains with respect to the atomic chain of pure Cu. The results indicate that if Co atoms are at the center of the atomic chain, then the shift in the energy of the ground state is larger, whereas if Co atoms are at the edges of the atomic chain then the shift in the energy of the first excited state becomes larger. In order to extract binding energy and the coupling between nearest neighbor atoms, a calculation based on the tight binding approximation was carried out. The binding energy of Cu and the coupling between Cu atoms were set at $\alpha = 3.31$ eV and $\gamma = -0.95$ eV, respectively [8]. The results of these calculations show that the binding energy of the Co atom is lower than the binding energy of the Cu atom ($\alpha_{Co} = 2.96 \pm 0.01$ eV). On the other hand, the coupling between Co–Cu is the same within the uncertainty of the calculation ($\gamma_{Co} = -0.94 \pm 0.05$ eV).

Figures 14(a) and (b) show the topography of Cu_3CoCu_4 and Cu_8 chains. The Co impurity, as mentioned above, appears higher than the neighboring Cu atoms (see figure 14(c)). Unlike the Pd impurities embedded in the Au chains, the Co atoms do not act like an impenetrable quantum wall and divide the Cu chain into two independent quantum wells; instead Co impurities cause asymmetries in the local density of states (LDOS) measured on the atomic chains. As an example, dI/dV curves measured on Cu_3CoCu_4, showing the ground state, the first and the second excited states, are presented in figures 14(d)–(g). LDOS curves are calculated using a method based on tight binding (see figure 14(h)). Comparison of figures 14(g) and (h) shows that the model suggested by the authors qualitatively reproduces the experimental results.

4. Self-assembled atomic chains

This section is devoted to the presentation of some examples of self-assembled atomic chains on various surfaces. The main advantage of self-assembly is the possibility of creating atomic chains that are literally defect free and hundreds of nanometers long. Up to now, tens of publications, if not hundreds, have reported the formation of self-assembled atomic chains of various elements on various surfaces (mostly on semiconductors). Among these atomic chains are Pt/Ge(001) [12], Au/Ge(001) [13], Au/Si(111) [36], In/Si(111) [37], Bi/Si(001) [15], and rare-earth nanowires on Si(001) [38].

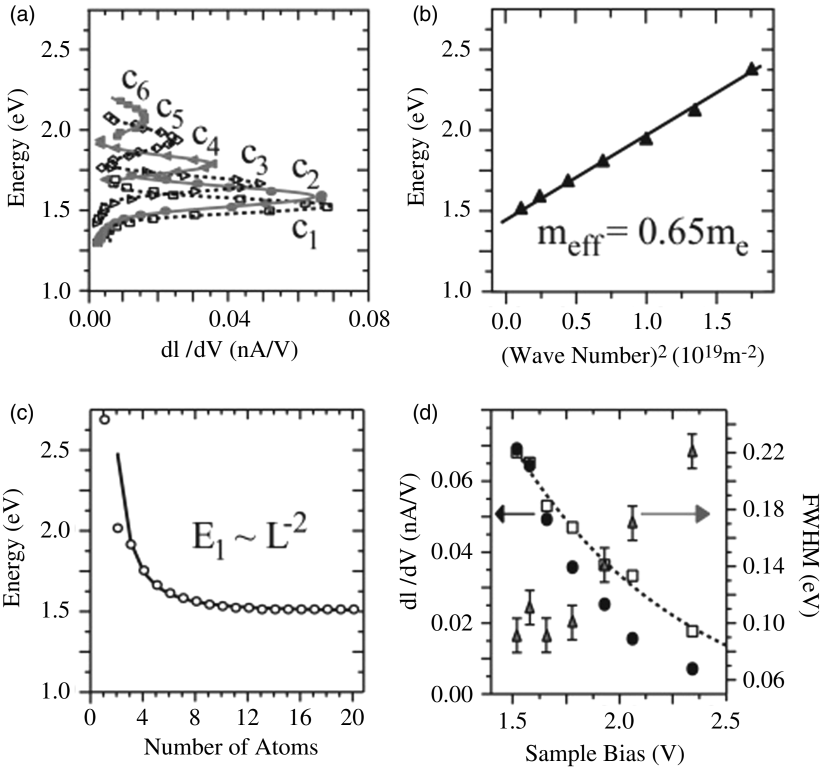

Figure 10. (a) Coefficients c_n from fitting $\mathrm{d}I/\mathrm{d}V$ oscillations in a Pd_{20} chain to a one-dimensional 'particle-in-a-box' model. Each maximum in c_n defines the position of a quantum well state in the chain. (b) Energy position of quantum well states as a function of squared wavenumber for Pd_{20} on NiAl(110). The slope of the linear fit to the data yields the effective electron mass of states in the quantum well. (c) Position of the lowest energy $\mathrm{d}I/\mathrm{d}V$ peak in Pd chains with increasing number of atoms. Data points were fitted with an L^{-2} dependence on the chain length L. (d) Width (▲), maximum $\mathrm{d}I/\mathrm{d}V$ intensity (●), and peak area in arbitrary units (□) of quantum well states in a Pd_{20} chain, derived from the bias-dependent coefficients c_n shown in (a). The dashed line is an exponential fit, illustrating the decrease of the $\mathrm{d}I/\mathrm{d}V$ peak area for states with higher quantum number n. Reprinted with permission from [33]. Copyright 2005 American Chemical Society.

In this review, we focus on atomic chains of Au and Pt. These atomic chains, being metallic and extremely stable in a wide temperature range, are promising candidates for technological applications. Before going into the details of recent studies of these atomic chains it is worth mentioning in a few words why Au and Pt, 5d transition metals, form atomic chains. In the literature it is well known that the reconstructions observed in the low indexed surfaces of these 5d fcc metals, e.g. Au, Pt, and Ir, are significantly different from the low indexed surfaces of the isoelectronic 4d transition metals [39]. The difference in the structure of these surfaces is attributed to the change in the bonding strength. In the transition metals with a nearly full d band, the bonding between atoms comes from the hybridization of the d and s electrons in the solid. Due to the relativistic effect in the 5d metals, the energy of the s band is lowered and therefore s bands lie closer to the d bands which enhances the strength of the hybridization of s and d bands [40]. This hybridization is weak in the non-relativistic 4d transition metals compared to the relativistic 5d transition metals. Another important factor that plays a role in the bonding strength is the extended geometry of 5d orbitals due to the better screening and slightly larger ion core. The stiffer bulk moduli and larger cohesive energy of the bulk 5d metals provide additional evidence for the existence of a stronger bond [41]. This stronger bonding can be the reason of the formation of these atomic chains. This idea is experimentally supported by the formation of Au chains on the Ge(001) surface. On the other hand, Ag atoms, having similar properties to Au (such as both of them being immiscible in Ge), do not form atomic chains [42]. Similarly, Pd, being a 4d transition metal, does not form atomic chains on Ge: instead Pd atoms form 3D alloy clusters [43]. This experimental evidence supports the idea that the increased binding strength of 5d transition metals causes the formation of these chains. In addition to this, it is not possible to rule out the fact that the majority of these self-assembled atomic chains are found on semiconductor surfaces which already have a tendency to form one-dimensional structures [44].

4.1. Topographical properties of Au and Pt atomic chains on a Ge(001) surface

In this section the topographical features of Au and Pt atomic chains formed on a Ge(001) surface are discussed. Si(001) and Ge(001) have basically the same crystal structure with very similar electronic properties. However, the extensive studies of the Au on Si(001) system do not indicate the formation of atomic chains; instead the Au on Si(001) system, depending on the growth and annealing temperatures, shows a number of different reconstructions. The differences between Au induced

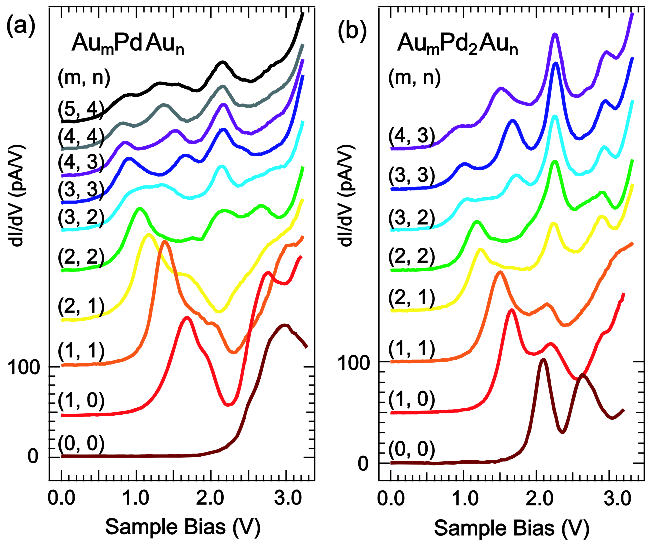

Figure 11. Evolution of localized resonances at impurities. (a) STS of a Au chain with a single Pd impurity acquired at each step of construction from isolated Pd atom to Au_5PdAu_4. Each spectrum was acquired with the tip directly above the Pd atom. (b) STS of a Au chain with a Pd dimer impurity acquired at each step of construction from isolated Pd_2 dimer to $Au_4Pd_2Au_3$. Each spectrum was acquired with the tip directly above the center of the Pd_2 dimer. The tip–sample distance was set with V_{sample} between 2.85 and 3.00 V and $I_{\text{tunnel}} = 1.00$ nA. Reprinted with permission from [34]. Copyright 2005, American Institute of Physics.

reconstructions of Ge and Si crystals are attributed to the reconstruction of Si(001) surface in response to the strain induced by foreign atoms [45–47].

A typical STM image of a clean Ge(001) terrace is shown in figure 16(a) [48]. In a terrace both the (2 × 1) and $c(4 \times 2)$ reconstructed domains are present [44, 49, 50]. The dimer row structure of Ge(001) surface rotates 90° on alternating terraces [51]. The high-resolution STM images of (4 × 2) and (2 × 1) reconstructed domains are shown in figures 16(b) and (c), respectively.

Figure 17(a) shows an STM image of the Ge(001) surface, after 0.5 ML of Au was deposited on the surface at 675 K. In this image, Au induced atomic chains are visible together with the clean Ge(001) surface. The length of the Au chains can reach several hundred nanometers. Anti-phase boundaries both parallel and perpendicular to the Au chains are indicated in this figure. Figures 17(b) and (c) show detailed images of the Au chains. Alternating white and gray rows make up the (4 × 2) reconstruction. Figure 17(d) shows the height profile measured between points A and B. The white chains are 0.13 nm higher than the Ge(001) dimer rows, whereas the gray chains are about 0.03 nm higher than the Ge terrace. Based on the STM images measured on Au chains a ball and stick model was proposed (see figure 18). In this model, white chains are considered to be formed by Au–Au dimers, whereas Au–Ge dimers form gray chains. The height difference between white and gray chains is attributed to the difference in the electron density of Au and Ge atoms near the Fermi level. STM images of these Au chains could be measured down to 0.2 V, indicating that the Au chains are metallic and the regions covered with these chains have a smaller band gap than the clean Ge(001) surface.

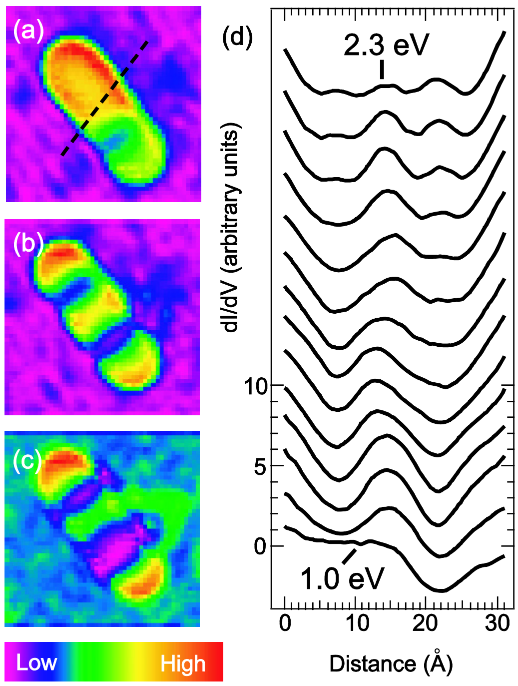

Figure 12. dI/dV images of the Au_5PdAu_4 chain taken at (a) 1.00 V, (b) 1.30 V, and (c) 1.60 V. Each curve in (d) is a cross section of a dI/dV image of the Au_5PdAu_4 chain. The dashed line in (a) illustrates the location of the cross sections. The cross sections are displayed in order of increasing V_{sample} from bottom ∼1.00 V to top ∼2.30 V in 0.10 V increments. The curves have been offset to facilitate comparison. The cross sections are displayed such that the four-atom Au segment is on the left-hand side. Reprinted with permission from [34]. Copyright 2005, American Institute of Physics.

On the other hand, upon Pt deposition, the Ge(001) surface undergoes a major transition leading to the formation of previously unknown terraces, called α and β. These terraces have distinctively different and rather interesting electronic and topographic features. The β terraces host Pt nanowires, one of the nicest examples of self-organized low-dimensional systems.

Once a clean Ge(001) surface is obtained, an equivalent of 0.25 ML (or higher amounts) of Pt is deposited onto the surface at room temperature. After Pt deposition the sample is annealed at 1050±25 K. Figure 19 shows a typical STM image of a Pt modified Ge(001) surface. The relative coverage of β terraces grows as the amount of Pt deposited on the surface increases.

Except for the cases of double steps, the step down of a β terrace is always an α terrace. However, occasionally a terrace can have both α and β terrace structures separated by a domain boundary (see figure 19). A recent study has shown that at 80 K, α terraces are semiconducting with a band gap of about 0.4 eV, whereas β terraces are metallic. STS measurements at the steps separating these two terraces show the formation of metal induced gap states [52].

Pt nanowires consist of dimerized Pt atoms. A recent density functional theory (DFT) study on the Pt nanowires showed that the dimerization of Pt atoms is a

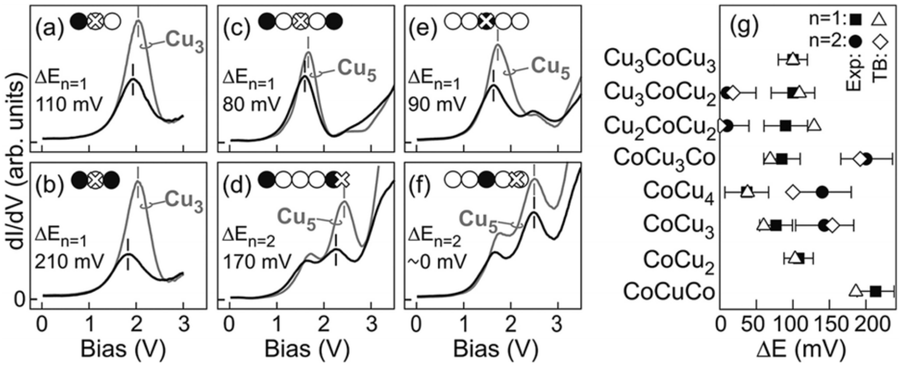

Figure 13. dI/dV spectra of Co–Cu chains comprising $N = 3$ ((a), (b)) and $N = 5$ atoms ((c)–(f)) indicated by black curves; sphere models show the chain structure with Co (Cu) atoms in black (white) and the tip position during dI/dV detection. Systematic downward shifts of ΔE in binding energy are observed for the ground state ($n = 1$) and the first excited state resonance ($n = 2$) relative to the simultaneously measured resonances of pure Cu$_N$ reference chains (gray curves). Panel (g) shows the resonance peak shifts ΔE observed for various Co–Cu chains (black symbols) compared to tight-binding-calculated values (open symbols). Set point current and bias 0.1 nA, 0.1 V; tip retraction prior to bias ramping at constant tip height 0.4 Å ((c),(d)) and 1.3 Å ((a),(b),(e),(f)); lock-in modulation amplitude and frequency 25 mV and 670 Hz. Reproduced with permission from [35]. Copyright 2007 by the American Physical Society.

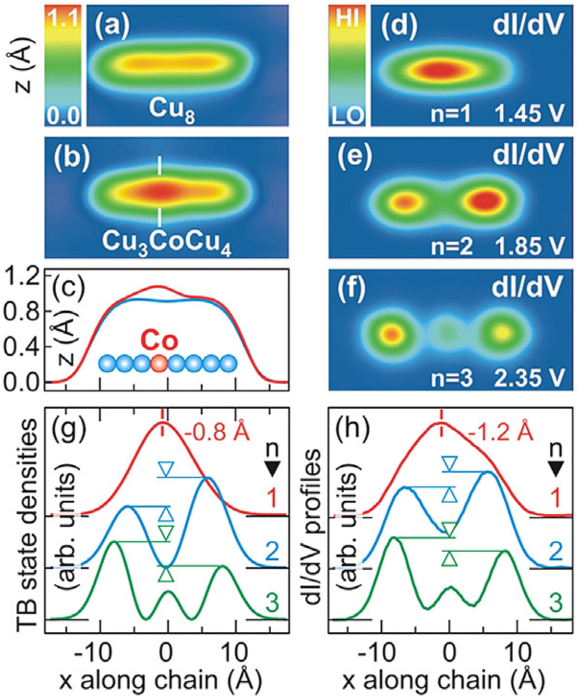

Figure 14. Constant current images (37 Å × 18 Å, 0.1 nA, 0.1 V) of a Cu$_8$ (a) and a Cu$_3$CoCu$_4$ chain (b) along with the corresponding height profiles (c). dI/dV maps (37 Å × 18 Å) of the ground state (d) and the first (e) and second excited state (f) of the Cu$_3$CoCu$_4$ chain. Basic features of the corresponding LDOS profiles measured along the chain axis (h) are qualitatively reproduced by the tight-binding-calculated state density profiles (g). Set point current and bias prior to dI/dV mapping at constant tip height: 0.1 nA, 0.2 V. Reproduced with permission from [35]. Copyright 2007 by the American Physical Society.

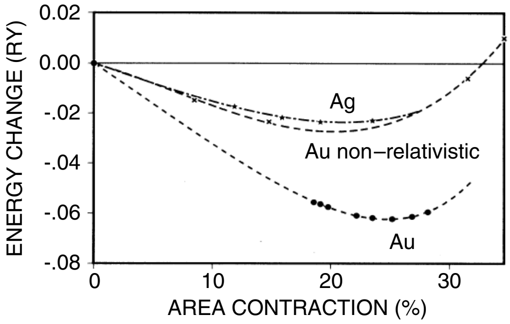

Figure 15. Energy change per atom for Au and Ag monolayers in close-packed arrangement as a function of percentage contraction of surface area per atom. Note that the energy gain reduces substantially if a non-relativistic potential is used for Au. Reproduced with permission from [40]. Copyright 1989 by the American Physical Society.

direct consequence of the significant lattice mismatch of the bulk Ge and Pt nearest neighbor distances (4.0 Å and 2.77 Å, respectively) and it is driven by Frenkel–Kontorova pairing [53]. The width of the trough between Pt nanowires is 1.6 nm, or higher integer multiples of 0.8 nm, i.e. 2.4 and 3.2 nm. Figure 20(a) is an STM image of a Pt nanowire patch where all the troughs have an equal width of 1.6 nm. On the other hand, the STM image shown in figure 20(b) is measured on a patch where the troughs between nanowires are 1.6 and 2.4 nm. A careful comparison of the regions enclosed by the rectangles in figure 20(b) reveals that when the width of a trough is 1.6 nm (2.4 nm) the dimerized Pt atoms of the nanowires are in registry (out of registry).

In order to explore the electronic structure of Pt nanowires, STS experiments have been performed extensively on different nanowire patches. In figure 21, two LDOS curves measured on 1.6 nm wide troughs at 300 and 80 K are presented. The difference between the LDOS curves is striking. The LDOS curve measured at 80 K has a peak located just above the Fermi level. The shape of the peak resembles the density of states of a one-dimensional state (van Hove singularity) which is proportional to $(E - E_n)^{-1/2}$, where E_n is the energy of this one-dimensional state [54].

However, the shape of the peak alone is insufficient to prove its one-dimensional character. Therefore, we have

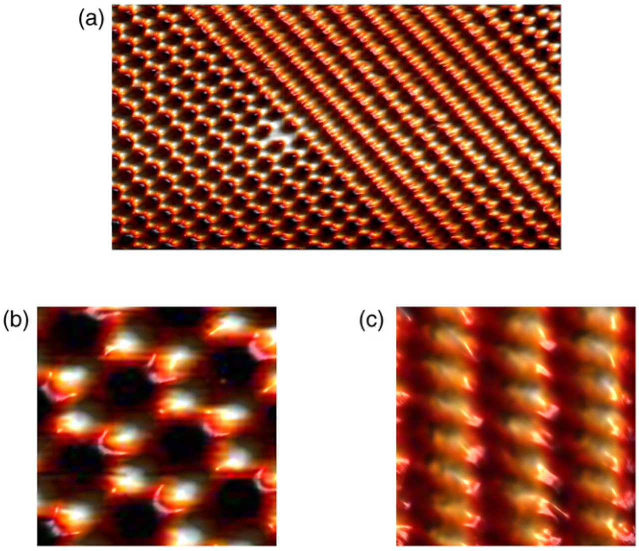

Figure 16. (a) A 15.25 nm × 7.65 nm STM image of a clean Ge(001) surface. Both 2 × 1 and $c(4 \times 2)$ domains are visible. (b) A 2.25 nm × 2.25 nm STM image of a $c(4 \times 2)$ domain of a clean Ge(001) surface. (c) A 2.25 nm × 2.25 nm STM image of a 2 × 1 domain of a clean Ge(001) surface. In all the images, the sample bias and the tunneling current are −1.5 V and 0.42 nA, respectively. All the images were recorded at 300 K. (Data from the PhD thesis of N Oncel, University of Twente, The Netherlands, courtesy of N Oncel.)

performed $\mathrm{d}I/\mathrm{d}V$ mapping of this state in order to determine the spatial location of this state on the surface.

Figure 22 shows the $\mathrm{d}I/\mathrm{d}V$ mapping of this one-dimensional state together with the topography. The state is located in the trough between the nanowires and runs parallel to the nanowires. In other words, the nanowires act as quantum walls and confine the state between them. However, we know that an inverted topography of the surface corrugation is superimposed on the $\mathrm{d}I/\mathrm{d}V$ map of a state, which means that the nanowires, being local protrusions in topography, should be depressions in $\mathrm{d}I/\mathrm{d}V$ mapping and similarly the troughs between the nanowires, being local depressions in topography, should be protrusions in $\mathrm{d}I/\mathrm{d}V$ mappings [55]. The first impression of the $\mathrm{d}I/\mathrm{d}V$ mapping of the surface seems to be in line with this assumption. However, a careful inspection reveals that on the trough there are defects due to missing atoms. For this type of defect, the $\mathrm{d}I/\mathrm{d}V$ signal should show an enhanced protrusion if what is measured is only an inverted topography. Moreover, the defects on the nanowires are also not only affecting the $\mathrm{d}I/\mathrm{d}V$ signal on the nanowires but are also destroying the local protrusions on the troughs close to these defective regions of the nanowires. Putting all these observations together suggests that the Pt nanowires provide a one-dimensional confining potential, with a confined state between them.

The simplest model to describe this behavior is a quantum well with impenetrable walls. The eigenvalues of energy are given by equation (1). This equation suggests a scaling law $(\frac{n^2}{L^2})$ for the eigenvalues of energy. The validity of this scaling

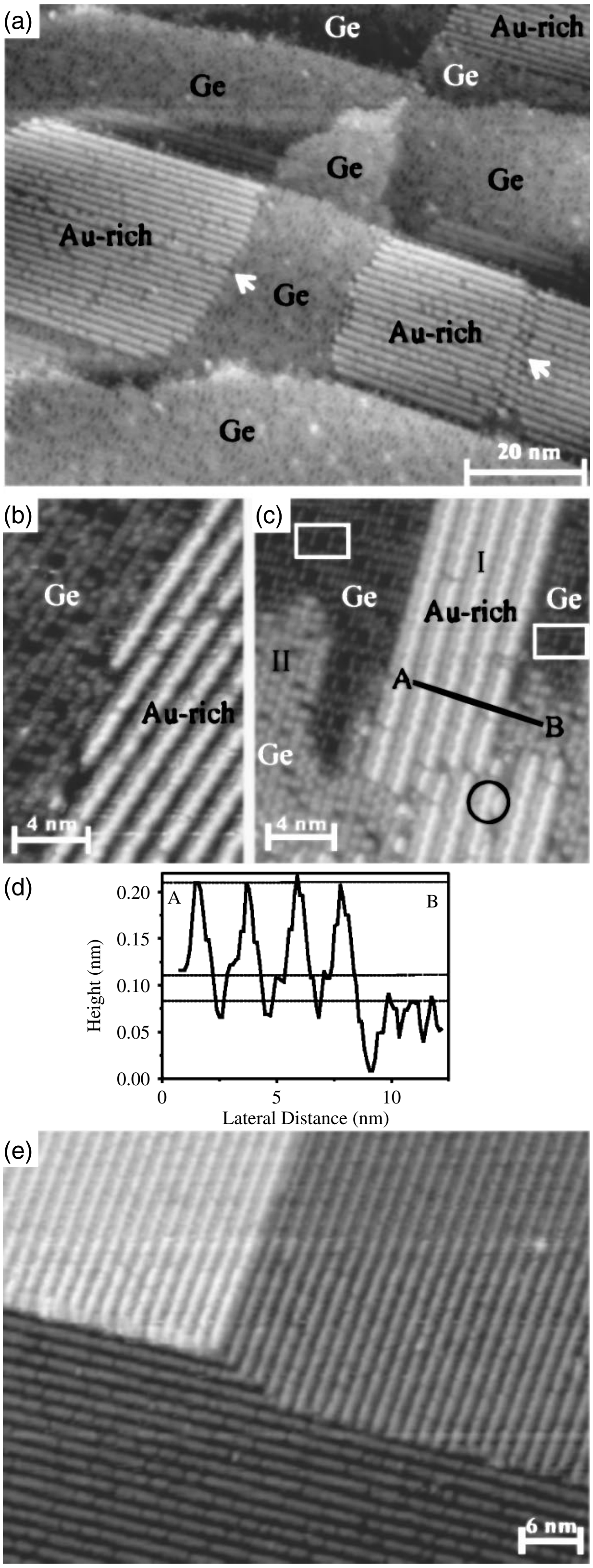

Figure 17. Large (a) and small (b) scale STM images obtained after depositing 0.5 ML Au on Ge(001) at a rate of 0.6 ML $\min^{-1}$ at 675 K. (c) STM image of 0.5 ML Au deposited on Ge(001) at 0.7 ML $\min^{-1}$ at 575 K. (d) Line profile obtained through AB in (c). (e) STM image of 1.5 ML Au deposited on Ge(001) at 675 K. Sample biases were: (a) −1.5 V, (b) −0.8 V, (c) −1.5 V, and (e) −1.5 V. Reprinted with permission from [12]. Copyright 2004 by the American Physical Society.

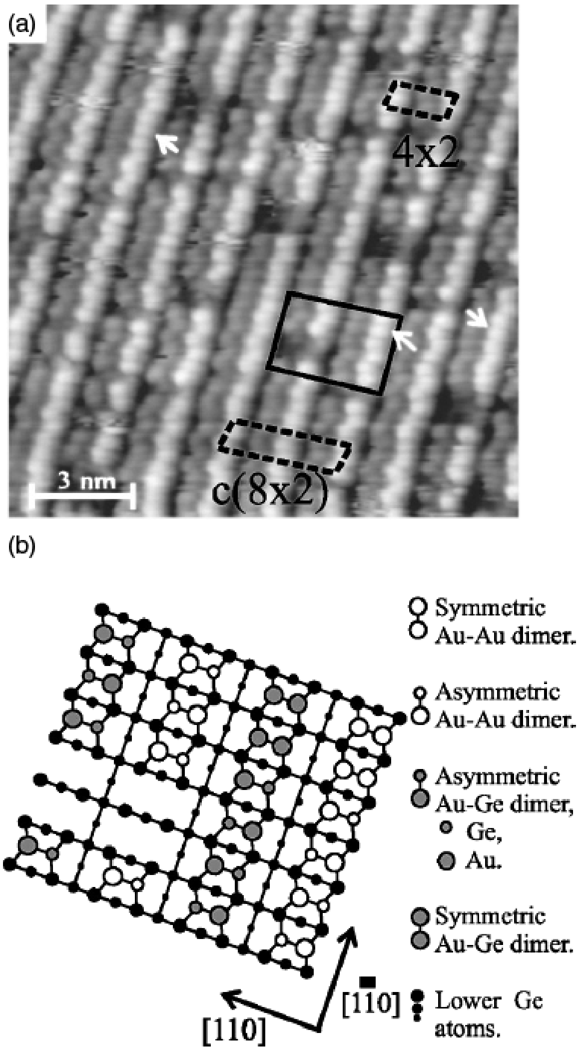

Figure 18. (a) High-resolution STM image of 1.5 ML of Au deposited on Ge(001) at a rate of 0.6 ML min^{-1} at 675 K; the sample bias was -0.7 V. (b) Ball-and-stick model for the region surrounded by the solid parallelogram in (a). Reprinted with permission from [12]. Copyright 2004 by the American Physical Society.

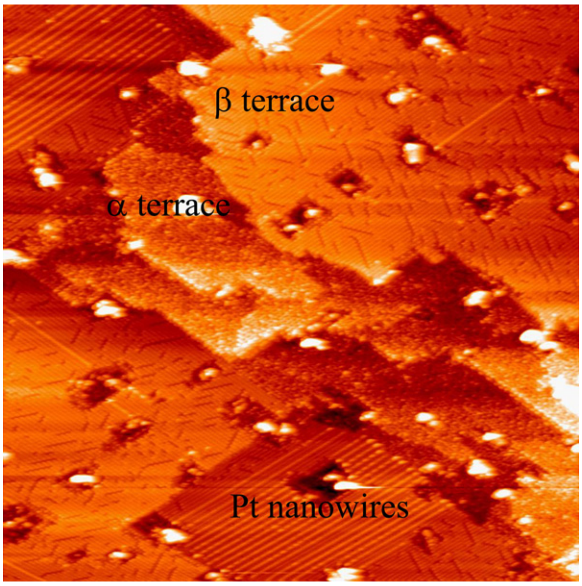

Figure 19. A 100 nm × 100 nm STM image of a Pt modified Ge(001) surface measured at 80 K. This particular region has a wide patch of Pt nanowires, and bare β and α terraces. The sample bias and the tunneling current are -1 V and 0.45 nA, respectively. (Data from the PhD thesis of N Oncel, University of Twente, The Netherlands, courtesy of N Oncel.)

law for the confined state can be tested by comparing the eigenvalues of troughs of different width. Figure 23 shows the LDOS curves measured on two troughs of different width. The LDOS curve measured on a 1.6 nm wide trough has only one eigenvalue and it is located at approximately 0.1 eV in the spectrum. On the other hand, the LDOS curve measured on a 2.4 nm wide trough has two eigenvalues located at 0.04 eV and 0.16 eV, respectively. Comparison of these three values clearly reveals that these eigenvalues obey the scaling law given above.

A quantum well with impenetrable walls can confine an infinite number of states. However, experimentally only one confined state for a 1.6 nm wide well and two confined states for a 2.4 nm wide well have been observed. This indicates that the walls of the quantum well formed by Pt nanowires are not infinitely high, but finite.

The eigenvalues of a quantum well with finite walls are classified into two groups, even and odd, which represent the number of nodes of the corresponding eigenfunctions. The ground state, which has no node, is an even solution:

$$\frac{\sqrt{\gamma - y^2}}{y} = \tan(y) \qquad \text{(even solutions)}$$

$$\frac{\sqrt{\gamma - y^2}}{y} = -\cot(y) \qquad \text{(odd solutions)}$$

where $\gamma = \frac{2\cdot m_{\text{eff}}\cdot V_0\cdot L_{\text{eff}}^2}{\hbar^2}$, $y = L_{\text{eff}}\sqrt{\frac{2\cdot m_{\text{eff}}\cdot E}{\hbar^2}}$, and $m_{\text{eff}} = \lambda\cdot m L_{\text{eff}} = \upsilon\cdot L$

Assuming that the height of the wall, V_0, the effective mass of the electron, m_{eff}, and the ratio of the effective barrier width to the topographical distance, υ, are the same for the 1.6 and 2.4 nm wide quantum wells, all three energy levels of the confined states can be fitted very well for $V_0 = 0.21$ eV and $\upsilon\sqrt{\lambda} = 0.8$. This model cannot be extended further to determine υ and λ and extract the effective mass of an electron and the effective width of the well independently. The predicted value of V_0 must be smaller than the $n = 2$ state for the 1.6 nm trough (0.4 eV), which explains why it is possible to measure this state.

In figure 24(a), the spatially averaged cross section of the ground state (the black dots) is presented together with an ideal ground state wavefunction (blue dots). On the other hand, figure 24(b) is the $\mathrm{d}I/\mathrm{d}V$ mapping of the exited state. The shape is rather different if we compare it with the ideal wavefunction (blue curve). This is due to the significant contribution of the tail of the ground state wavefunction to the $\mathrm{d}I/\mathrm{d}V$ peak of the exited state. This intermixing of the states is also visible in the LDOS curve shown in figure 23. The intermixing is due to the broadening of the peaks. This broadening of the peaks has two origins,

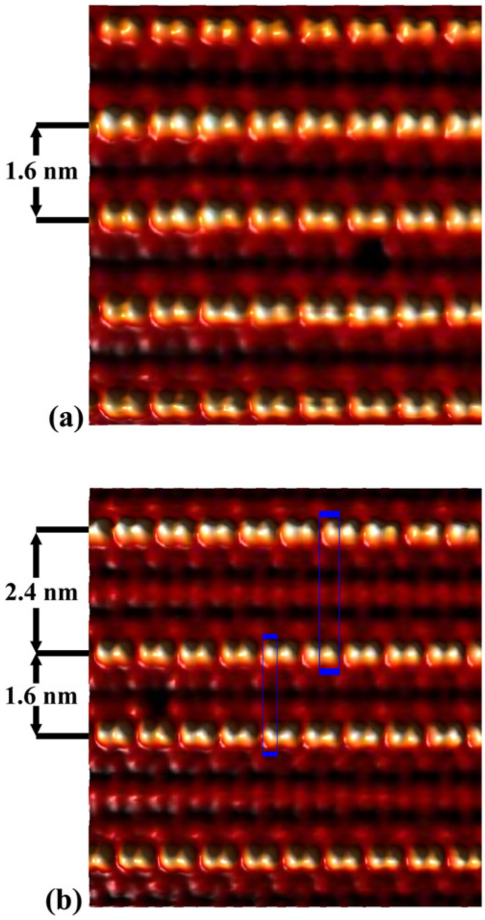

Figure 20. (a) A 6.75 nm × 6.75 nm STM image of a patch of five nanowires. The width of the troughs between the nanowires is 1.6 nm. (b) A 7.9 nm × 7.9 nm STM image of a patch of Pt nanowires. In this STM image, both 1.6 and 2.4 nm wide troughs are visible. The rectangles are drawn to guide the eye and indicate the phase relations between neighboring nanowires. The sample bias and the tunneling current are −1.2 V and 0.44 nA, respectively. Both images were recorded at 80 K. (Data from the PhD thesis of N Oncel, University of Twente, The Netherlands, courtesy of N Oncel.)

thermal and experimental. Experimental broadening is due to the modulation voltage of 10 mV used while measuring dI/dV curves. Assuming a negligible intrinsic peak width, the broadening, W, is defined as

$$W = [(3.6kT)^2 + (2.5V_{\mathrm{mod}})^2]^{1/2}.$$

In this case the total broadening is about 35 meV, which agrees well with the observed shape of the spectra. In order to resolve the wavefunction of the exited state the contribution of the ground state wavefunction should be subtracted. The dotted line in figure 24(b) shows the corrected wavefunction of the exited state.

A recent study of Pt nanowires showed that the one-dimensional states confined in the trough between Pt nanowires are not the only exotic phenomena that this surface offers. Using scanning tunneling microscopy and spectroscopy, it is shown that Pt nanowires undergo a phase transition from a 2× periodicity at room temperature to a 4× periodicity at low temperature (see figure 25).

In a one-dimensional system, a Peierls transition above 0 K is possible only if the system loses its ideal one-dimensional character through coupling with the substrate and the neighboring one-dimensional systems. Figures 26(a) and (b) show STM images measured on a patch of nanowires and an isolated nanowire at 4.7 K, respectively. The nanowires labeled a–c in figure 26(a) show a 4× periodicity, whereas the nanowire lying at the edge of the patch (labeled d) and the isolated nanowire (labeled e) shows a 2× periodicity. The absence of a phase transition in the isolated Pt nanowires and the location of the Pt nanowires at the edge of a patch suggest that the weaker neighbor coupling of these Pt nanowires favors the ideal one-dimensional character of these nanowires and therefore lowers the transition temperature below 4.7 K [53].

4.2. Au chains on vicinal Si(111) surfaces

Au-induced reconstruction and Au chain formation has been observed in various vicinal Si(111) surfaces [56–59]. The vicinal Si(111) surfaces offer a few advantages as a substrate. The most important advantage is the possibility of forming extensively long kink-free steps. This is due to the fact that the unit cell of the Si(111) surface is large and the creation of

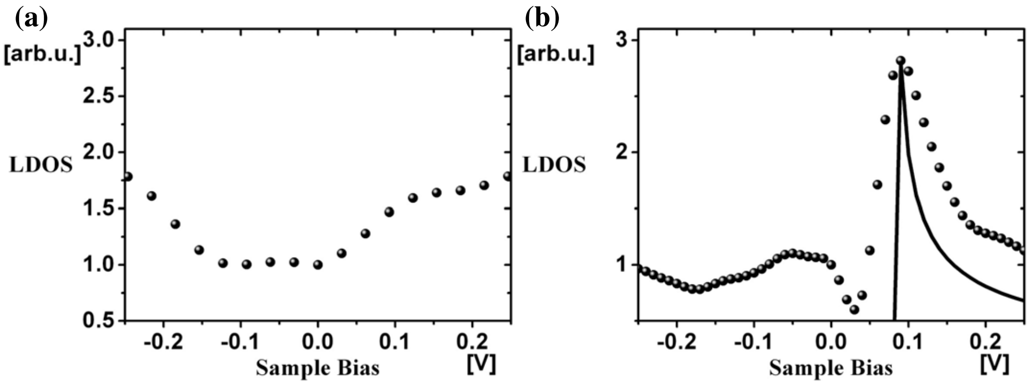

Figure 21. (a) LDOS curve measured at a 1.6 nm wide trough at 300 K. (b) An LDOS curve measured at a 1.6 nm wide trough at 80 K. The solid line is the ideal one-dimensional density of state located at 0.09 eV. (Data from the PhD thesis of N Oncel, University of Twente, The Netherlands, courtesy of N Oncel.)

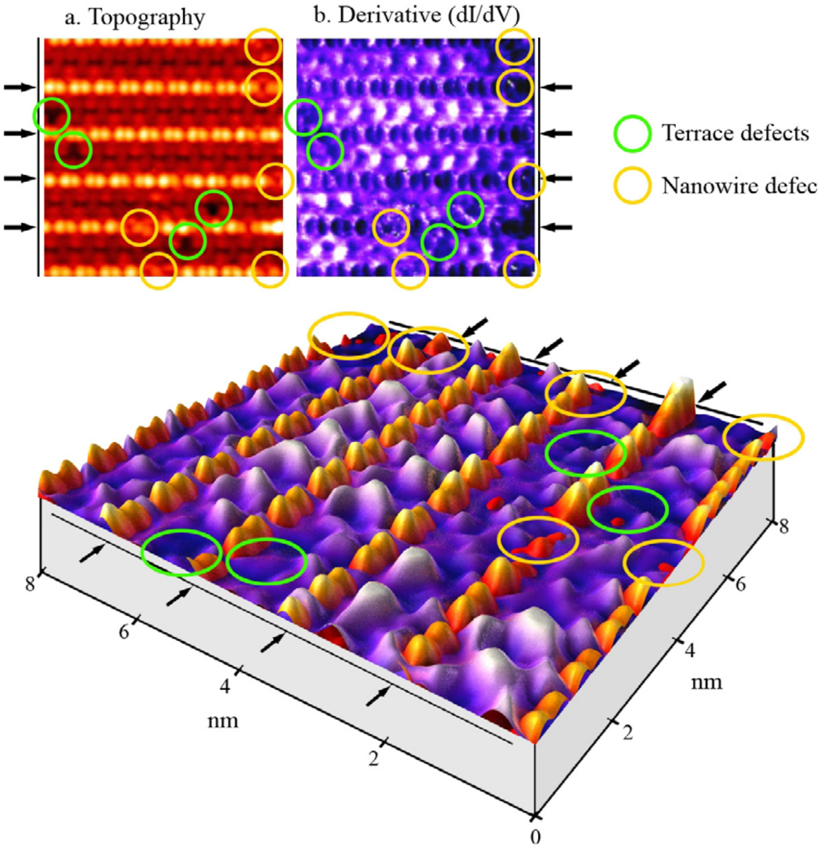

Figure 22. Topography (a) and spatial map of the differential conductivity (dI/dV) (b) of a 8 nm × 8 nm area with several Pt nanowires recorded at $T = 77$ K. The sample bias is 0.15 V and the tunnel current is 0.437 nA. The dI/dV map is recorded with a modulation voltage of 10 mV and an oscillation frequency of 797 Hz (this frequency exceeds the bandwidth of the feedback loop). In the lower image a three-dimensional representation of the topography (orange) and dI/dV map (purple) is shown. The one-dimensional electronic state is exclusively located in the troughs of the Pt nanowires (black arrows refer to the position of the Pt nanowires). The yellow and green circles (ellipses) refer to defects in the Pt nanowire and underlying substrate, respectively. The confinement of the electronic state disappears near these defects. Reproduced with permission from [54]. Copyright 2005 by the American Physical Society.

a kink on the step edge requires many extra atoms [60, 61]. Au chains formed on vicinal Si(111) surfaces lie parallel to the step edges and reach lengths of hundreds of nanometers. This allows one to study the properties of these atomic chains with a wide variety of experimental techniques and makes them feasible candidates for technological applications. Another advantage of using vicinal Si(111) surfaces is the ability to control the electronic structure of the surface surrounding the atomic chains by changing the tilt direction and tilt angle of the surface. For example, changing the tilt direction of the Si(111) surface from $[\bar{1}\bar{1}2]$ to $[11\bar{2}]$ reduces the number of broken bonds at the step edge from two to one. On the other hand, by changing the tilt angle, the width of the terraces and therefore the separation between nearest neighbor Au chains can be adjusted.

4.2.1. Si(111)-(5 × 2)–Au. The Si(111)-(5 × 2)–Au surface forms upon Au deposition on the flat Si(111) surface. Figure 27 shows typical STM images of this surface. The formation of the Si(111)-(5 × 2)–Au surface requires deposition of exactly 0.4 ML of Au [62]. In figure 27(a), the surface still has some terraces in the Si(111)-(7 × 7) structure, indicating that the deposited Au is insufficient. On the other hand, in figure 27(b), the surface has a terrace with $\sqrt{3} \times \sqrt{3}$-Au patches indicating that an excess amount of Au is deposited. Usually, low energy electron diffraction is used to calibrate the deposition of exactly 0.4 ML of Au.

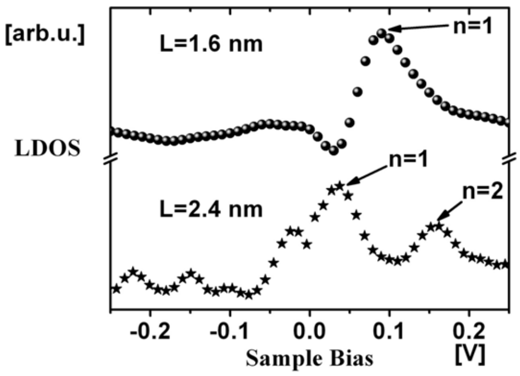

Figure 23. This figure shows two LDOS curves measured in 1.6 and 2.4 nm troughs. The positions of the eigenvalues are indicated with arrows and n is the quantum number of the indicated state. (Data from the PhD thesis of N Oncel, University of Twente, The Netherlands, courtesy of N Oncel.)

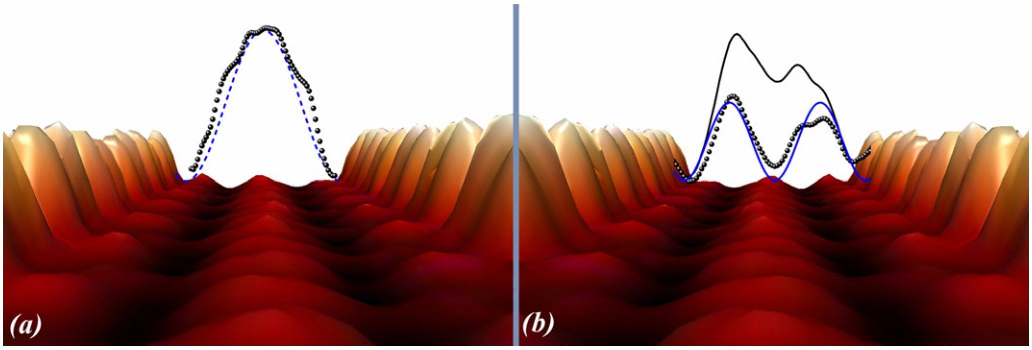

Figure 24. (a) The black dotted line is the spatially averaged cross section of the differential conductivity of the ground state of a 2.4 nm wide trough. The blue dotted line shows the expected squared wavefunction. (b) The black line is the spatially averaged cross section of the differential conductivity of the first exited state of a 2.4 nm wide trough. The black dotted line shows a corrected distribution, in which the contribution of the ground state is subtracted from the measured distribution. The blue dotted line shows the expected squared wavefunction. The asymmetry between the two peaks of the confined state is attributed to the asymmetry of the trough and the nanowires forming the walls of the well. (Data courtesy of N Oncel, University of Twente, The Netherlands.)

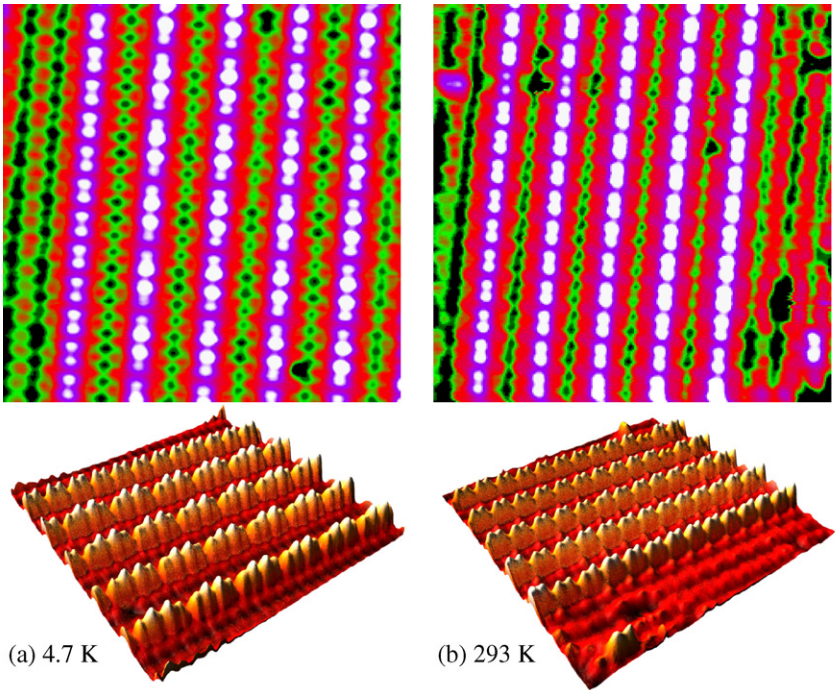
(a) 4.7 K
(b) 293 K

Figure 25. STM images (2D and 3D) of an array of Pt chains recorded at 4.7 K (a) and 293 K (b). At 4.7 K the outermost left chain (near the edge of an array) exhibits a 2× periodicity while the dimers of the Pt chain within an array buckle alternatly up and down, leading to a 4× periodicity. At room temperature every chain shows a 2× periodicity. The image size is 10 nm × 10 nm, bias voltage is −1.5 V and the tunneling current is 0.5 nA (for both images). Reproduced with permission from [53]. Copyright 2008 Elsevier.

Figure 28 shows the angle-resolved photoemission spectra measured at ∼16 K on bare Si(111) and Si(111)-(5 × 2)–Au surfaces [63]. As expected, the spectrum of the Si(111)-7 × 7 surface has two surface states located at 0.1 eV (from adatoms) and 0.7–0.8 eV (from rest atoms) below the Fermi level. On the other hand, the spectrum of the Si(111)-(5 × 2)–Au surface has only one peak. The absence of any dispersion with the photon energy (22 eV $\leqslant h\nu \leqslant$ 48 eV) indicates that the peak originates from the surface. Additional proof showing that the peak belongs to a surface state comes from the location of the peak in the spectrum since the peak is located within the band gap of the Si bulk projected on the (111) plane.

Figure 29(a) shows the angle-resolved photoemission spectra measured parallel to the Au chains. The relatively high band width (0.95 ± 0.03 eV) suggests strong coupling of the orbitals of individual atoms forming the chain, whereas low effective mass ($m = 0.5m_e$) at the bottom of the band indicates high mobility. Angle-resolved photoemission measurements performed perpendicular to the chain show smaller dispersion at both the band minimum (0.14 ± 0.03 eV) and the band maximum (0.03 ± 0.03 eV).

The dispersion relation of the surface state is shown in figure 29(c.) The band does not cross the Fermi level as in the case of highly stepped Si(111)-(5 × 1)–Au, instead the

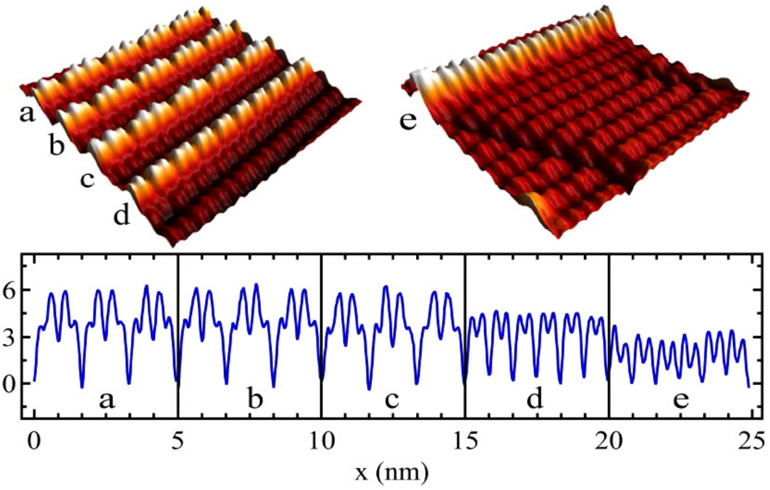

Figure 26. STM images of an array of Pt chains (left image) and an isolated Pt chain (right image) recorded at 4.7 K. Line scans along the Pt chains labeled a–e are depicted below the STM images. Isolated Pt chains (chain e) located near the edge of an array (chain d) exhibit a 2× periodicity, whereas the Pt chains within the patch (chains a–c) show a 4× periodicity. The image size is 10 nm × 10 nm, the bias voltage is −1.5 V, and the tunneling current is 0.5 nA. Reproduced with permission from [53]. Copyright 2008 Elsevier.

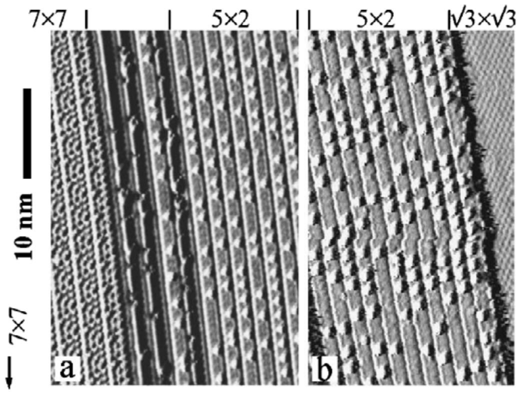

Figure 27. Optimization of surfaces and coverage calibration using STM. The Au coverage for flat Si(111)-5 × 2–Au is twice as large as for stepped Si(557)–Au (0.4 ML versus 0.2), indicating two Au rows versus one. (a) Si(111)-5 × 2–Au: insufficient Au coverage leads to patches of clean 7 × 7. (b) Si(111)-5 × 2–Au: excess Au coverage leads to patches of $\sqrt{3} \times \sqrt{3}$–Au. The sample bias is −1 V for (a) and (b). Reproduced with permission from [62]. Copyright 2001 by the American Physical Society.

band is curved down and opens up a gap at the Fermi level at the location of the zone boundary. Due to the opening of this band gap at the zone boundary we may associate the gap with a Peierls instability.

Before studying the existence a Peierls transition, it is necessary to prove that the band is actually one-dimensional. Figure 29 shows a two-dimensional map of the photoemission spectra. At the bottom of the band (−1.3 eV) the constant energy contour is diagonal, indicating that the band has both $k_\parallel$ and $k_\perp$ dependence. Therefore, the bottom of the band is two-dimensional. On the other hand, at the top of the band (−0.24 eV) the constant energy contour is parallel to the x-axis, showing that the band has only $k_\parallel$ dependence, indicating that the top of the band is one-dimensional. Another important feature to extract from figure 30(c) is that this one-dimensional band lies very close to the zone boundary ($\mathrm{ZB}^{n\times2}$). Based on these two experimental results, it was suggested that the states lying at the top of the band are responsible for the observed Peierls instability [64, 65].

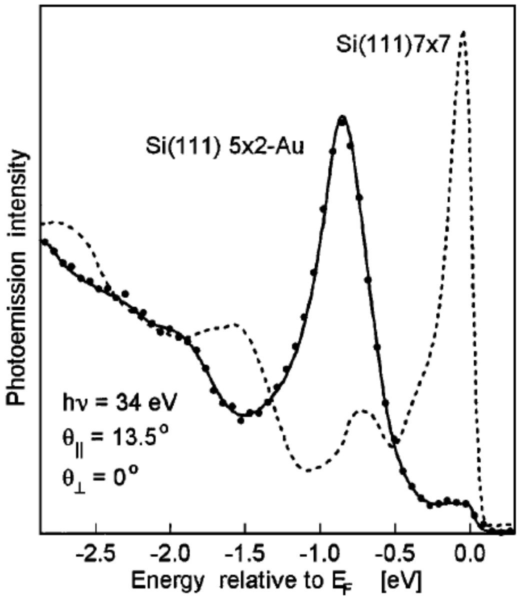

Figure 28. Angle-resolved photoemission spectrum from the Si(111)-5 × 2–Au chain structure compared to the Si(111)-(7 × 7) substrate. The (7 × 7) adatom state at E_F is replaced by a Au induced surface state below E_F. Reproduced with permission from [63]. Copyright 2000 by the American Physical Society.

4.2.2. Si(557)–Au. The advantage of using the stepped Si surface is the existence of additional anisotropy at the surface which allows formation of atomic chains along the step edge direction. Another advantage is being able to change the inter-chain distance by changing the tilt angle of

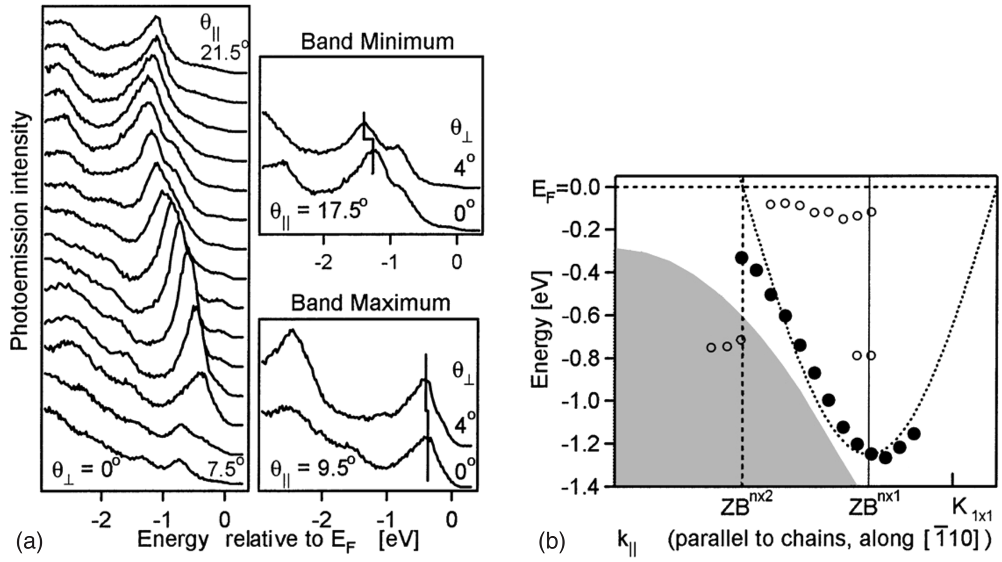

Figure 29. Band dispersion of the Au-induced state on Si(111)-5 × 2–Au. The panels in (a) provide raw data in the directions parallel and perpendicular to the chains ($\theta_\parallel$ along $[\bar{1}10]$ and $\theta_\perp$ along $[11\bar{2}]$). The surface state (solid circles) can be approximated by a half-filled band (dotted curve). However, it circumvents the Fermi level via doubling of the periodicity along the chain from 5 × 1 to 5 × 2 and opening a Peierls gap at the new zone boundary $\mathrm{ZB}^{n\times 2}$. Reproduced with permission from [63]. Copyright 2000 by the American Physical Society.

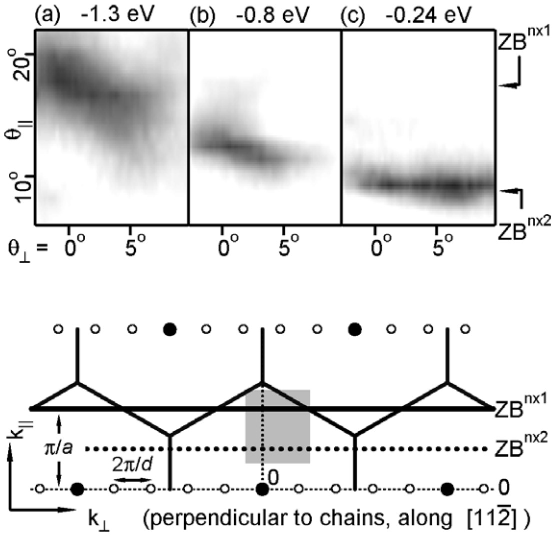

Figure 30. Top: Constant energy contours in k space for the surface state on Si(111)-5 × 2–Au, obtained from angular photoemission distributions at $h\nu = 34$ eV (high intensity shown dark). The emission at the bottom of the band in (a) spreads diagonally in both $\vec{k}$ directions, indicating two-dimensional behavior. The horizontal contour at the top of the band in (c) is one-dimensional, because it does not depend on $k_\perp$. It coincides with the period-doubled zone boundary $\mathrm{ZB}^{n\times 2}$, suggesting that it has triggered a Peierls gap. Bottom: The one-dimensional Brillouin zone of a single chain, compared to the surface Brillouin zone (hexagonal lines, solid circles) and a 5 × 1 diffraction pattern (open circles). The zone boundaries are $\mathrm{ZB}^{n\times 1}$ and $\mathrm{ZB}^{n\times 2}$ before and after doubling the period a along the chain. The gray rectangle represents the $\vec{k}$ range of panels (a)–(c). Reproduced with permission from [63]. Copyright 2000 by the American Physical Society.

the surface. Si(557)–Au is an especially important example since it is one of the first, and one of the most controversial, atomic chains studied so far. Below, a model of the surface structure is introduced. The inter-chain spacing (19 Å) is significantly larger than the spacing between Au atoms in a chain (3.83 Å), therefore it is possible to consider Au chains as one-dimensional structures. On the terrace of the Si(557)–Au surface, besides Au chains Si adatoms form a chain structure too (see figures 31 and 32).

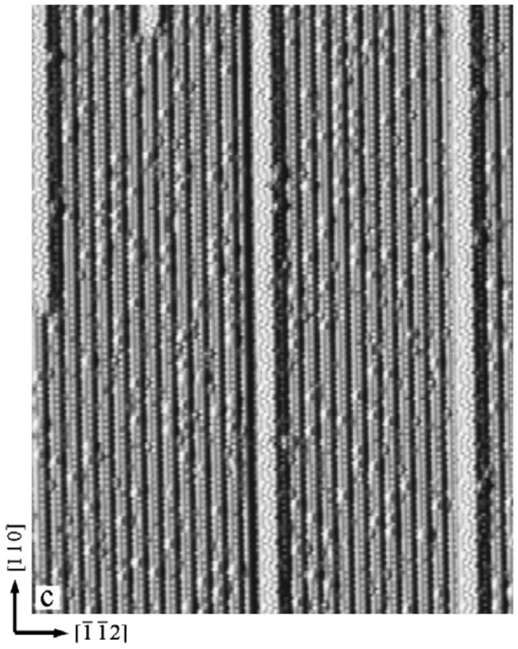

Figure 31. Si(557)–Au: insufficient Au coverage leads to Si(111)7 × 7 stripes one unit cell wide. The sample bias is 2 V. Reproduced with permission from [62]. Copyright 2001 by the American Physical Society.

Figure 33(a) shows the photoemission spectra of the Au induced state measured along the Au chains. The peak

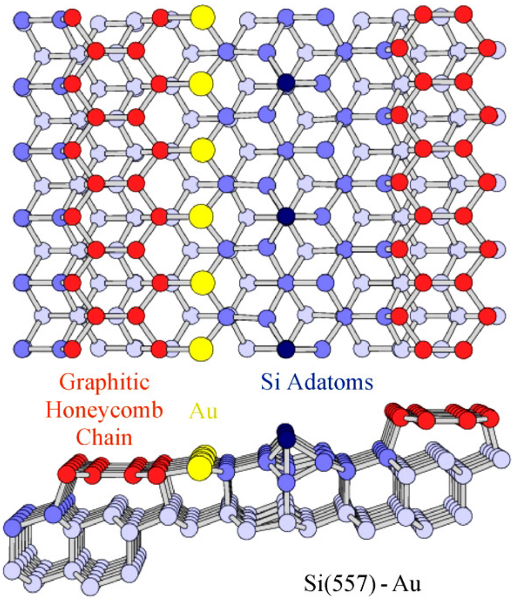

Figure 32. The structural elements of Au induced chain structures on vicinal Si(111) surfaces, demonstrated by a model of the Si(557)–Au surface obtained from x-ray diffraction [61] and total energy calculations [66]. The key element driving these one-dimensional chain structures is the honeycomb chain, a strip of graphitic Si surface atoms (red). The Au chain (yellow) is located at the center of the terrace in substitutional sites, contrary to expectations from step flow growth. Reproduced from [70]. Copyright 2007 Elsevier.

attributed to this state disappears in the range of $-10^\circ \leqslant \theta_e \leqslant 10^\circ$; however, the dispersion relation of the state extracted from the photoemission data shows the metallic character of the state (see figure 33(b)). The angle-resolved photoemission spectra were measured as a function of the k vector perpendicular ($k_\perp$) to Au chains. The absence of any $k_\perp$ dependence proved that the Au-induced state is one-dimensional (see figure 33(c)). The form of the photoemission spectra and the dispersion relation of the peak did not show any indication of the formation of a Peierls type of temperature dependent transition. The one-dimensional nature of the state and relatively higher energy cutoffs at the Fermi level were considered as indications of the formation of a Luttinger liquid [13]. The theory of one-dimensional electron systems predicts that the spectrum of a Luttinger liquid obeys a power law [26, 27] (see also figure 5). However, for this system, the calculated power, α, is significantly large, suggesting unrealistically strong and long ranged interactions. One of the reasons for the significantly large α is considered to be due to the defects and impurities on the Au chains. Another reason was attributed to the large sample area ($\sim$1 mm^2) measured with photoemission experiments. In such a large region, the surface photo-voltage created by the reduced recombination rate at low temperature may show variations which may eventually lead a change in the measured spectrum around the Fermi level.

A detailed angle-resolved photoemission spectrum near the Fermi level shows two peaks emerging from a single peak while moving away from the Fermi level, and these two peaks recombine near the near the Brillouin zone (see figure 33(d)). These experimental findings led authors to assign these two peaks as spinon and holon excitations.

However, the higher resolution photoemission experiments performed on the Si(557)–Au surface showed that the splitting of the bands attributed to spinons and holons do not converge at the Fermi level. Figure 34(a) shows the photoemission intensities of these two states near the Fermi level around $k_\parallel = 0.4$ Å^{-1} [67]. This splitting in the bands rules out the possibility of a Luttinger liquid [68]. Energy distribution curves (EDC) of photoemission intensity for S1 and S2 states are used to check the spectral shape of each band near the Fermi level. The EDC of state S1 shows a typical metallic behavior with the Fermi level located at the middle of the leading edge of the EDC. This result shows that state S1 does not obey the power law behavior of a Luttinger liquid. On the other hand, state S2 does not exhibit any clear Fermi cutoff for all $k_\parallel$ values. At the k_F value (i.e. 0.41 Å^{-1}), the leading edge of its EDC is moved from the Fermi level to 0.05 eV above the Fermi level, which could be attributed to the Luttinger liquid or defect induced Coulomb shift [69]. Initial photoemission studies show no clear Fermi cutoff at 12 K. This discrepancy suggests that there might be a temperature dependent change in the spectral weight around the Fermi level. In order to study this, photoemission experiments were performed down to 70 K. The results showed no temperature dependence in the dispersion [67], as noted previously [13]. At low temperatures, surface photo-voltage effects gain importance and need to be compensated. The results after compensating the photo-voltage effects show that the leading edge of state S1 gradually moves to higher binding energies at lower temperatures whereas the edge of state S2 remains almost constant. This observation was attributed to the opening of a gap of about 80 meV (based on the assumption of a symmetric gap). This result also explains why Segovia *et al* did not observe a clear Fermi cutoff at 12 K in the previous study.

STM images of the Si(557)–Au surface show only two Si chains and no Au chain. The bound state between Au atoms and neighboring Si atoms were well below the Fermi level, and therefore the states of the Au chains are not accessible with STM. The role of Au atoms on the surface is nothing but a catalyst to form the observed reconstruction on the surface [70]. Because of this, the states discussed so far were attributed to the Si atoms on the surface. One of them is formed at the step edge (denoted by α) and the other one is an adatom chain (denoted by β) formed on the terrace. From the comparison of the STM images measured at 300 and 78 K, a phase transition from 1× to 2× modulations is observed on α-type chains. The existence of the phase transition suggests that the metallic state (S1) originates from the chains of Si atoms along the step edge. On the other hand, it is not possible to assign an origin for the S2 band from these experiments. The absence of any phase transition in the S2 band is attributed to a critical temperature above 300 K. The Fermi level crossing of S2 is closer to the zone center, indicating a stronger electron–phonon coupling. This also supports the possibility of having a phase transition above 300 K.

A new controversy emerged when a theory paper suggested a completely different origin for the band splitting

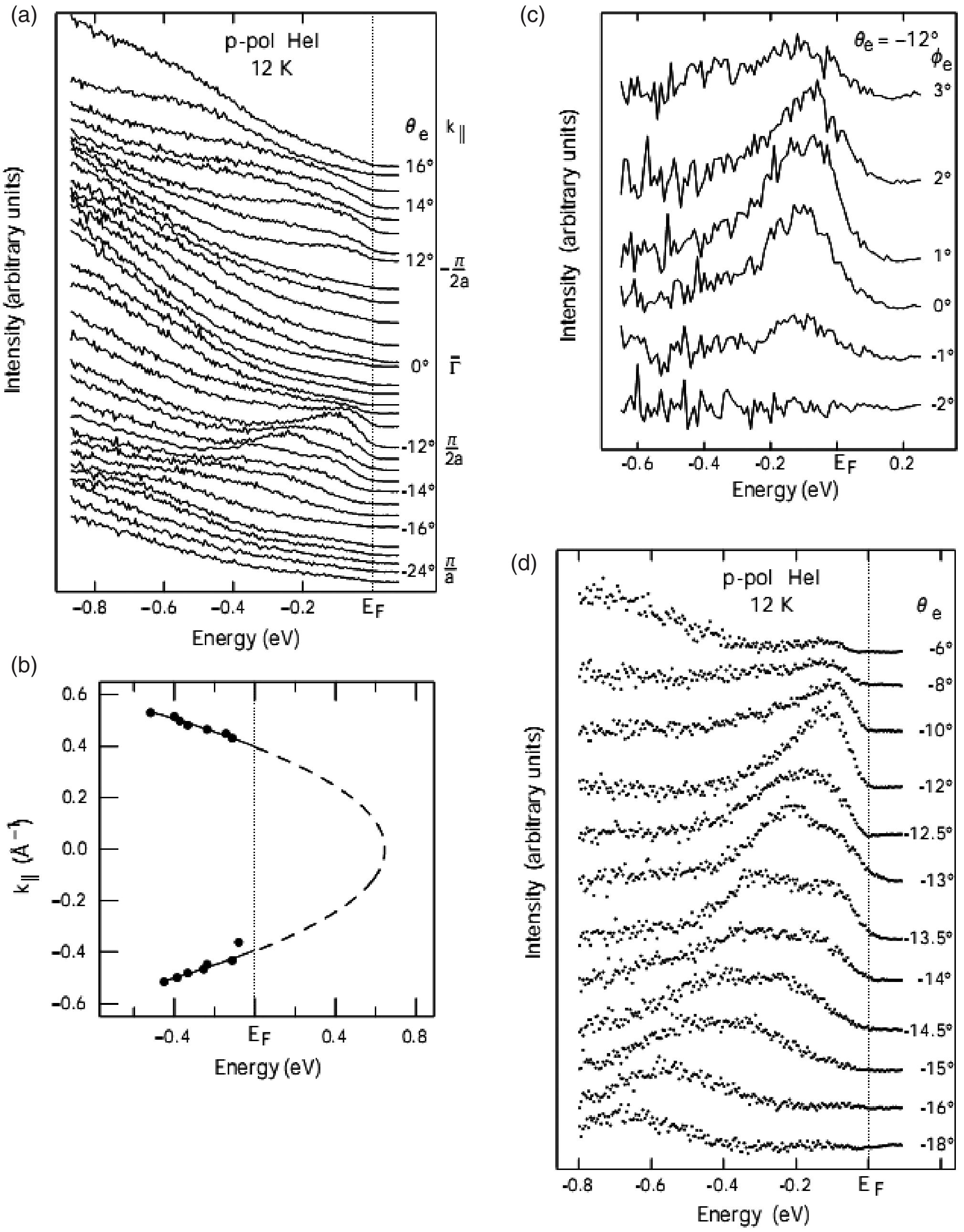

Figure 33. Dispersion of the Au-induced state parallel to the chains. (a) Angle-resolved photoemission spectra of Si(111)-5 × 1 Au, with the surface wavevector, $\vec{k}_\parallel$, along the chain direction [1$\bar{1}$0]. The polar emission angle θ_e is noted with respect to the surface normal. The angular steps between spectra for which the value of θ_e is marked on the figure are equal. $\vec{k}_\parallel$ values are given for emission at E_F, with a being the inter-Au distance within a chain, 3.83 Å. The electric vector of the radiation is contained in the emission plane (p-pol). In order to compensate for effects due to the polarization of the exciting radiation, negative angle spectra are multiplied by a factor of of 0.75. An excitation feature is clearly seen dispersing towards zero energy as normal emission is approached. (b) The energy and momentum positions of the main structure plotted and plotted to a parabola showing the characteristic dispersion of a metallic band. (c) Angle-resolved photoemission spectra with varying surface wavevector $\vec{k}_\parallel$ perpendicular to the chains. The polar angle θ_e in the emission plane is fixed at −128 and the angle ϕ_e in the perpendicular plane is varied. In order to remove any visual distortions coming from the featureless background in the raw spectra; this has been subtracted. The lack of dispersion in this direction confirms the one-dimensional nature of the system under study. (d) Detailed angle-resolved photoemission spectra of Si(111)-5 × 1 Au for θ_e between −68 and −188. To emphasize the structures of interest, a featureless background has been removed as explained in the text. The double-peaked structure observed in the range θ_e − 13 to −15 is assumed to originate from the excitation of spin and charge collective modes. The spinon lies closest to E_F, and the holon at deeper energy. Reproduced with permission from [13]. Copyright 1999 from Macmillan Publishers.

at the Fermi level [71]. Their explanation is based on the existence of spin–orbit coupling. The effect of spin–orbit splitting on Au-induced surface states has been shown by angle-resolved photoemission experiments and calculations [72, 73]. The temperature dependent change in topography of the α chains is attributed to buckling of the step

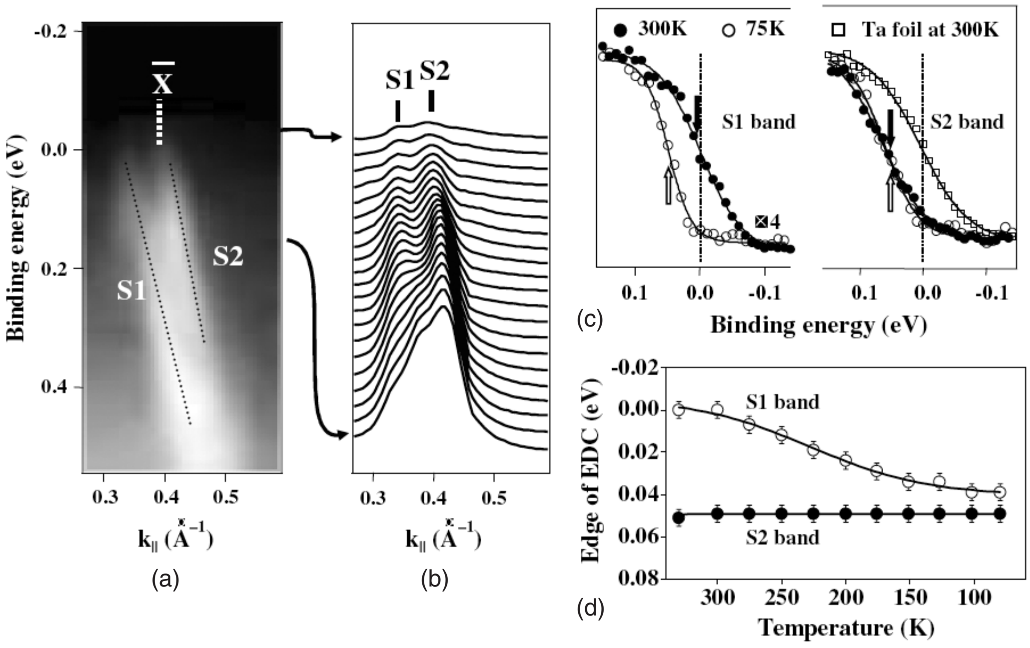

Figure 34. Two highly dispersive S1 and S2 bands of Au/Si(557) at 300 K as shown (a) in the photoelectron intensity map in gray scale as a function of binding energy (as referenced to E_F) and momentum along the one-dimensional chains $k_{\parallel}$ and (b) in the momentum distribution curves of the photoelectron intensity. (c) Energy distribution curves (EDCs) of the photoemission intensity for bands S1 and S2 at the two k_F positions of 0.35 and 0.41 Å^{-1}, respectively, and (d) temperature dependence of the center-of-the-leading-edge positions of EDCs (see the arrows in (c)) for S1 and S2 at the corresponding k_F positions. The EDC of a typical normal metal, Ta, is given for comparison in (c) and, due to the low intensity of S1 at E_F, its EDC in (c) is enlarged by a factor of 4. Reproduced with permission from [67]. Copyright 2003 by the American Physical Society.

edge. At room temperature, the atoms forming the α chain oscillate between up and down configurations. Therefore, STM images only reflect the time averaged position of these atoms. However, at low temperature the oscillations are suppressed, which allows clear imaging of individual atoms.

Figure 36(a) shows the equilibrium structure of a Si(557)–Au surface. The model is similar to the models suggested before [74]. Figure 36(b) (36(c)) show the band structure of the surface parallel to the step edge calculated with non-spin-polarized (spin-polarized) VASP [75, 76] using the local density approximation. In this graph the unoccupied (occupied) band shown with triangles are originating from the adatoms (rest atoms). On the other hand, the atoms at the step edge, having two dangling bonds pointing perpendicular to the step edge, give rise to the flat band marked with open squares. The states originating from Au–Si bonds form two bands with rather different dispersion relations. The Au–Si(D) band is rather flat whereas the Au–Si(C) bond is dispersive. The shape and width of the dispersion of this last band and its spin–orbit splitting are consistent with the angle-resolved photoemission spectra experiments.

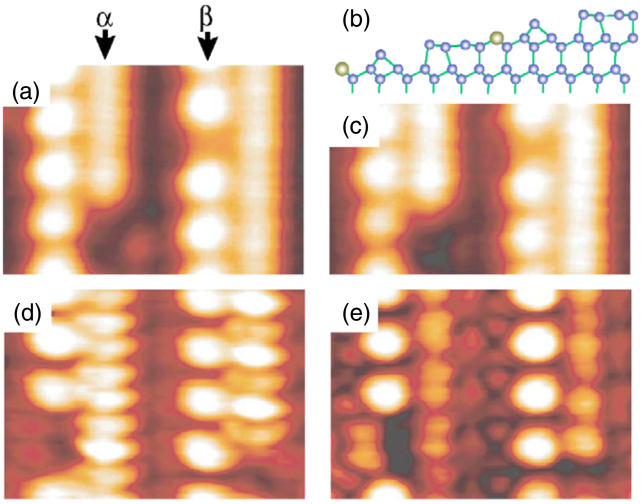

Figure 35. Empty-state STM images at (a), (c) 300 and (d), (e) 78 K with a sample bias of (a), (d) $V_s = 1.0$ and (c), (e) 0.7 V. The recent structural model of Au/Si(557) [16, 17, 19] is shown schematically in (b), where the large and small circles denote Au and Si atoms, respectively. Reproduced with permission from [67]. Copyright 2003 by the American Physical Society.

5. Outlook

The ability to manufacture atomic chains of various atoms in various sizes has given us the opportunity to study the oddities in one-dimensional physics. However, considering the fact that these studies summarized above exemplify a rather small portion of the total studies, the popularity of atomic chains among scientists cannot only be attributed to the natural curiosity of scientists wanting to investigate unexplored corners of the nano-world. In the near future, we will have reached the level where we incorporate individual atoms into devices. Therefore, studying the physics of

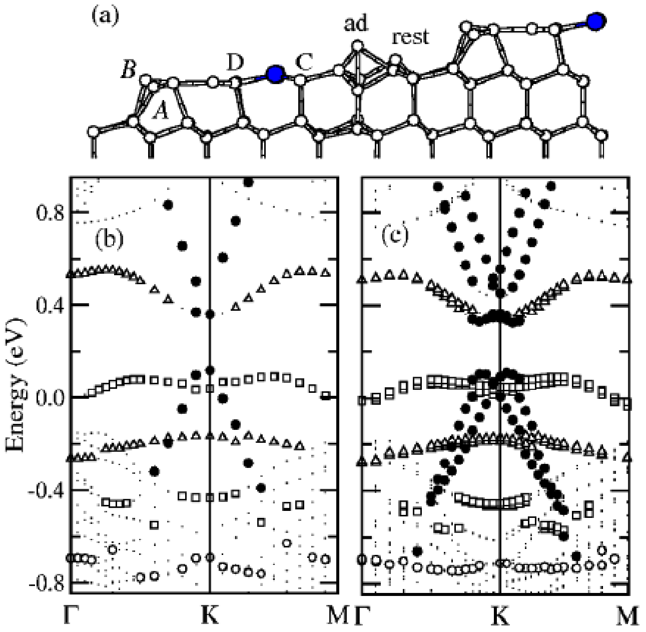

Figure 36. (a) Calculated equilibrium structure of the Si(557)–Au reconstruction. The corresponding electronic band structure is shown for a calculation not including (b), and including (c), the spin–orbit interaction. Energies are referred to the Fermi level. Surface states have been marked with different symbols according to their main atomic character (see text). Reproduced from [71]. Copyright 2004 by the American Physical Society.

these one-dimensional atomic chains has great importance for future technological applications. On the other hand, it is apparent that the functions of these atomic chains are not going to be limited to interconnectors of various components of an integrated circuit. One major opportunity, overlooked up to now, is to employ atomic chains as templates or bases (bottom-up approach) for manufacturing hierarchically higher order structures [77]. In this way, the size and the sharpness of the edges of the individual features can approach the angstrom level, well below the limits of the top-down approach.

Another rather important opportunity can come from chemical properties of these atomic chains. The catalytic properties of materials depends strongly on their size and dimensionality, therefore highly organized one-dimensional atomic chains can be employed as catalysts of various important reactions.

Without a doubt, the unknowns of the physical and chemical properties of one-dimensional atomic chains are going to fascinate more scientists and draw them into the world of nanowires.

Acknowledgments

I would like to thank Professors H J W Zandvliet and S Bernasek for their careful reading and helpful comments during the preparation of the manuscript. I would also thank the authors who allowed me to reproduce the figures used in this article. This work is partially supported by the National Science Foundation, Division of Chemistry, CHE-0616457.

References

[1] Marrian C R K and Tennant D M 2003 *J. Vac. Sci. Technol.* A **21** S207
[2] Peierls R E 1955 *Quantum Theory of Solids* (London: Oxford University Press)
[3] Luttinger J M 1963 *J. Math. Phys.* **4** 1154
[4] Crommie M F, Lutz C P and Eigler D M 1993 *Science* **262** 218
[5] Heller E J, Crommie M F and Lutz C P 1994 *Nature* **369** 464
[6] Wallis T M, Nillius N and Ho W 2002 *Phys. Rev. Lett.* **89** 236802
[7] Folsch S, Hyldgaard P, Koch R and Ploog K H 2004 *Phys. Rev. Lett.* **92** 056803
[8] Zankovych S, Hoffmann T, Seekamp J, Bruch J U and Torres C M S 2001 *Nanotechnology* **12** 91
[9] Hallback A S, Oncel N, Huskens J, Zandvliet H J W and Poelsema B 2004 *Nano Lett.* **4** 2393
[10] Tao F and Bernasek S L 2005 *J. Am. Chem. Soc.* **127** 12750
[11] Gurlu O, Adam O A O, Zandvliet H J W and Poelsema B 2003 *Appl. Phys. Lett.* **83** 4610
[12] Wang J, Li M and Altman E I 2004 *Phys. Rev.* B **70** 233312
[13] Segovia P, Purdie D, Hengsberger M and Baer Y 1999 *Nature* **402** 504
[14] Baski A A, Saoud K M and Jones K M 2001 *Appl. Surf. Sci.* **182** 216
[15] Miki K, Bowler D R, Owen J H G, Briggs G A D and Sakamato K 1999 *Phys. Rev.* B **59** 14868
[16] Nogami J, Liu B Z, Katkov M V, Ohbuchi C and Birge N O 2001 *Phys. Rev.* B **63** 233305
[17] Kittel C 1996 *Introduction to Solid State Physics* 7th edn (New York: Wiley)
[18] van Hove L 1953 *Phys. Rev.* **89** 1189
[19] Gasiorowicz S 1995 *Quantum Physics* 2nd edn (New York: Wiley)
[20] Ashcroft Neil W and David Mermin N 1976 *Solid State Physics* Thomson Learning
[21] Bruus H and Flensberg K 2004 *Many-Body Quantum Theory in Condensed Matter Physics: An Introduction* (USA: Oxford University Press)
[22] Mattuck R D 1976 *A Guide to Feynman Diagrams in the Many-Body Problem* 2nd edn (USA: Mac Grew-Hill)
[23] Giamarchi T 2004 *Quantum Physics in One Dimension* (New York: Oxford University Press)
[24] Sprunger P T, Petersen L, Plummer E W, Lægsgaard E and Besenbacher F 1997 *Science* **275** 1764
[25] Egger R and Graberth H 1995 *Phys. Rev. Lett.* **75** 3505
[26] Haldane F D M 1981 *J. Phys. C: Solid State Phys.* **14** 2585
[27] Voit J 1994 *Rep. Prog. Phys.* **57** 977
[28] Giuliani G and Vignale G 2005 *Quantum Theory of the Electron Liquid* (Cambridge: Cambridge University Press)
[29] Yao Z, Postma H W C, Balents L and Dekker C 1999 *Nature* **402** 273
[30] Peierls R E 1974 *Quantum Theory of Solids* (London: Oxford University Press)
[31] Nilius N, Wallis T M and Ho W 2002 *Science* **297** 1853
[32] Nilius N, Wallis T M, Persson M and Ho W 2003 *Phys. Rev. Lett.* **90** 196103
[33] Nilius N, Wallis T M and Ho W 2005 *J. Phys. Chem.* B **109** 20657
[34] Wallis T M, Nilius N, Mikaelian G and Ho W 2005 *J. Chem. Phys.* **122** 011101
[35] Laguate J, Nacci C and Fölsch S 2007 *Phys. Rev. Lett.* **98** 146804
[36] O' Mahony J D, McGilp J F, Flipse C F J, Weightman P and Leibse F M 1994 *Phys. Rev.* B **49** 2527
[37] Nogami J, Park S-I and Quate C F 1987 *Phys. Rev.* B **36** 6221
[38] Owen J H G, Miki K and Bowler D R 2006 *J. Mater. Sci.* **41** 4568 and the relavent references therein

[39] van Hove M A, Koestner R J, Stair P C, Biberian J P, Kesmodel L L, Bartos I and Somorjai G A 1981 *Surf. Sci.* **103** 189

[40] Takeuchi N, Chan C T and Ho K M 1989 *Phys. Rev. Lett.* **63** 1273

[41] Ho K M and Bohnen K P 1987 *Phys. Rev. Lett.* **59** 1833

[42] Chan L H and Altman E I 2006 *Phys. Rev.* B **66** 155339

[43] Wang J, Li M and Altman E I 2006 *J. Appl. Phys.* **100** 113501

[44] Zandvliet H J W, Swartzentruber B S, Wulfhekel W, Hattink B J and Poelsema B 1998 *Phys. Rev.* B **57** R6803

[45] Kageshima M, Torii Y, Tano Y, Takeuchi O and Kawazu A 2001 *Surf. Sci.* **472** 51

[46] Hild R, Meyer Zu Heringdorf F-J, Zahl P and Horn-von Hoegen M 2000 *Surf. Sci.* **454** 851

[47] Lin X F, Wan K J, Glueckstein J C and Nogami J 1993 *Phys. Rev.* B **47** 3671

[48] Oncel N 2007 Scanning tunneling microscopy and spectroscopy studies on Pt-modified Ge(001) and metallic (Pd,Au)-Quantum dots on self assembled monolayers *PhD Thesis* University of Twente Enschede, The Netherlands

[49] Zandvliet H J W 2003 *Phys. Rep.* **388** 1

[50] Gurlu O, Zandvliet H J W and Poelsema B 2004 *Phys. Rev. Lett.* **93** 066101

[51] Zandvliet H J W, Swartzentruber B S, Wulfhekel W, Hattink B and Poelsema B 1998 *Phys. Rev.* B **57** R6803

[52] Oncel N, van Beek W J, Poelsema B and Zandvliet H J W 2007 *New J. Phys.* **9** 449

[53] van Houselt A, Gnielka T, Aan de Brugh J M J, Oncel N, Kockman D, Heid R, Bohnen K P, Poelsema B and Zandvliet H J W 2008 *Surf. Sci.* **602** 1731

[54] Oncel N, van Houselt A, Huijben J, Hallback A S, Gurlu O, Zandvliet H J W and Poelsema B 2005 *Phys. Rev. Lett.* **95** 116801

[55] Bonnell D A 2000 *Scanning Probe Microscopy and Spectroscopy: Theory, Techniques, and Applications* (New York: Wiley–VCH)

[56] Hill I G and McLean A B 1997 *Phys. Rev.* B **55** 15664

[57] Collins I R, Moran J T, Andrews P T, Cosso R, O'Mahony J D, McGilp J F and Margaritondo G 1995 *Surf. Sci.* **324** 45

[58] Robinson I K, Bennett P A and Himpsel F J 2002 *Phys. Rev. Lett.* **88** 096104

[59] Jalochowski M, Strozak M and Zdyb R 1997 *Surf. Sci.* **375** 203

[60] Viernow J, Lin J L, Petrovykh D Y, Leibsle F M, Men F K and Himpsel F J 1998 *Appl. Phys. Lett.* **72** 948

[61] Lin J L, Petrovykh D Y, Viernow J, Men F K, Seo D J and Himpsel F J 1998 *J. Appl. Phys.* **84** 255

[62] Altmann K N, Crain J N, Kirakosian A, Lin J L, Petrovykh D Y, Himpsel F J and Losio R 2001 *Phys. Rev.* B **64** 035406

[63] Losio R, Altmann K N and Himpsel F J 2000 *Phys. Rev. Lett.* **85** 808

[64] Erwin S C 2003 *Phys. Rev. Lett.* **91** 206101

[65] McChesney J L, Crain J N, Perez-Dieste V, Zheng F, Gallagher M C, Bissen M, Gundelach C and Himpsel F J 2004 *Phys. Rev.* B **70** 195430

[66] Crain J N, McChesney J L, Zheng F, Gallagher M C, Snijders P C, Bissen M, Gundelach C, Erwin S C and Himpsel F J 2004 *Phys. Rev.* B **69** 125401

[67] Ahn J R, Yeom H W, Yoon H S and Lyo I-W 2003 *Phys. Rev. Lett.* **91** 196403

[68] Losio R, Altmann K N, Kirakosian A, Lin J-L, Petrovykh D Y and Himpsel F J 2001 *Phys. Rev. Lett.* **86** 4632

[69] Starowicz P, Gallus O, Pillo Th and Baer Y 2002 *Phys. Rev. Lett.* **89** 256402

[70] Barke I, Rugheimer T K, Zheng F and Himpsel F J 2007 *Appl. Surf. Sci.* **254** 4

[71] Sanchez-Portal D, Riikonen S and Martin R M 2004 *Phys. Rev. Lett.* **93** 146803

[72] LaShell S, McDougall B A and Jensen E 1996 *Phys. Rev. Lett.* **77** 3419

[73] Petersen L and Hedegard P 2000 *Surf. Sci.* **459** 49

[74] Sanchez-Portal D and Martin R M 2003 *Surf. Sci.* **532** 655

[75] Kresse G and Hafner J 1993 *Phys. Rev.* B **47** 558

[76] Kresse G and Furthmüller J 1996 *Phys. Rev.* B **54** 11169

[77] Oncel N, van Beek W J, Huijben J, Poelsema B and Zandvliet H J W 2006 *Surf. Sci.* **600** 4690